Article

Multi-parametric atlas of the pre-metastatic liver for prediction of metastatic outcome in early-stage pancreatic cancer

A list of authors and their affiliations appears at the end of the paper

Metastasis occurs frequently after resection of pancreatic cancer (PaC). In this study, we hypothesized that multi-parametric analysis of pre-metastatic liver biopsies would classify patients according to their metastatic risk, timing and organ site. Liver biopsies obtained during pancreatectomy from 49 patients with localized PaC and 19 control patients with non-cancerous pancreatic lesions were analyzed, combining metabolomic, tissue and single-cell transcriptomics and multiplex imaging approaches. Patients were followed prospectively (median 3 years) and classified into four recurrence groups; early (<6 months after resection) or late (>6 months after resection) liver metastasis (LiM); extrahepatic metastasis (EHM); and disease-free survivors (no evidence of disease (NED)). Overall, PaC livers exhibited signs of augmented inflammation compared to controls. Enrichment of neutrophil extracellular traps (NETs), Ki-67 upregulation and decreased liver creatine significantly distinguished those with future metastasis from NED. Patients with future LiM were characterized by scant T cell lobular infiltration, less steatosis and higher levels of citrullinated H3 compared to patients who developed EHM, who had overexpression of interferon target genes (*MX1* and *NR1D1*) and an increase of CD11B^{+} natural killer (NK) cells. Upregulation of sortilin-1 and prominent NETs, together with the lack of T cells and a reduction in CD11B^{+} NK cells, differentiated patients with early-onset LiM from those with late-onset LiM. Liver profiles of NED closely resembled those of controls. Using the above parameters, a machine-learning-based model was developed that successfully predicted the metastatic outcome at the time of surgery with 78% accuracy. Therefore, multi-parametric profiling of liver biopsies at the time of PaC diagnosis may determine metastatic risk and organotropism and guide clinical stratification for optimal treatment selection.

Pancreatic cancer (PaC) is an aggressive malignancy, with rising incidence[1] and a high rate of metastatic disease. Less than 25% of cases are amenable to potentially curative resection, and, of those, only 21% of patients survive to 5 years[1,2]. Liver metastasis (LiM) develops in over 40% of patients within the first 3 years after surgery and is almost uniformly fatal within months of its occurence[2,3]. Extrahepatic metastasis (EHM) occurs mainly in the peritoneum and lung, with isolated lung metastases correlating to less aggressive disease[2,3]. The inability to

predict the risk of subsequent LiM or EHM in patients with otherwise undetectable metastatic disease and effectively treat it represent major challenges in the management of PaC. Furthermore, the biologic determinants of organotropism, within the primary tumor and metastatic organs, remain largely undefined. Here we show that, in patients with localized PaC, peri-operative liver biopsies reveal liver alterations consistent with a pre-metastatic niche before overt metastatic colonization. Thus, we extensively characterized the molecular, cellular and

e-mail: dcl2001@med.cornell.edu

metabolic alterations in PaC pre-metastatic livers and developed a liver biopsy-based model that predicted future sites of distant recurrence: early LiM (within 6 months after resection), late LiM (more than 6 months after resection), EHM or no evidence of disease (NED). This classification schema could identify patients who benefit more from surgery versus neoadjuvant therapy (NAT).

Pre-metastatic livers of patients with PaC exhibit inflammation

To determine pre-metastatic niche features in livers of patients with PaC, we analyzed the molecular, cellular and metabolic profiles of intraoperatively collected liver biopsies from patients with localized, resectable PaC ($n = 49$) and non-PaC controls ($n = 19$) who underwent pancreatectomy without receipt of any NAT (Fig. 1 and Supplementary Table 1). Two pathologists independently evaluated the liver biopsies by histology and p53 immunostaining (Supplementary Fig. 1) to confirm the absence of micrometastases. Bulk liver tissue mRNA sequencing (mRNA-seq) identified 79 differentially expressed genes (DEGs) that were significantly altered in PaC livers compared to non-PaC livers, including upregulation of cell migration-inducing and hyaluronan-binding proteins (*KIAA1199/CEMIP*), matrix metalloproteinase-7 (*MMP7*), lysyl oxidase-like 4 (*LOXL4*), V-set domain-containing T cell activation inhibitor 1 (*VTCN1/B7-H4*), triggering receptor expressed on myeloid cells 2 (*TREM2*), Toll-like receptor 7 (*TLR7*) and Ki-67 (*MKI67*) (Fig. 2a and Supplementary Table 2). Gene set enrichment analysis (GSEA; Supplementary Table 3 and Supplementary Dataset 1) highlighted 'interferon response' and 'allograft rejection' as significantly enriched gene sets in PaC (Fig. 2b). DEGs upregulated in PaC were prominent in immune cell gene clustering[4], suggesting enhanced 'monocyte and lymphocyte chemotaxis' in PaC pre-metastatic livers[5] (Fig. 2c,d).

Intriguingly, patients with the most robust upregulation of immune-related genes (Fig. 2a) subsequently developed metastasis, in contrast to patients with PaC without recurrence over follow-up (NED) who displayed fewer differences in expression of these genes compared to non-PaC patients. In addition, the livers of patients with PaC with distant recurrence at any site featured five significantly enriched gene sets, involving inteferon alpha response as well as potential proliferation and regeneration mechanisms (such as 'E2F signaling' and 'spermatogenesis') compared to NED (Supplementary Table 4 and Supplementary Dataset 1).

We hypothesized that, at the time of resection, the livers of patients with PaC would display features that either promoted or counteracted subsequent metastasis and correlate with metastatic outcome. Thus, we separated patients with PaC with distant recurrence into LiM and EHM groups (Extended Data Table 1 and Fig. 1). Although no significant differences were observed in bulk liver gene expression between LiM and NED groups, comparison of EHM and NED groups identified 59 DEGs (Fig. 2e and Supplementary Table 5), with immune-related genes and pathways being the most highly enriched in the livers of the EHM group (Extended Data Fig. 1a and Supplementary Table 6).

These results suggest that EHM transcriptomic changes may reflect an anti-metastatic phenotype within the liver, as patients with EHM seemed to be 'resistant' to LiM during follow-up despite developing metastatic disease elsewhere. We used the EHM gene signature (Supplementary Table 5) to perform unsupervised hierarchical clustering of all patients with PaC and noted that a cohort of patients with LiM clustered with the patients with EHM (Fig. 2e), with recurrence at a timeframe that was much longer than the median of LiMs (7 months after resection). Of the 23 patients who developed LiM as the first site of recurrence, there was a clear separation between the 10 patients who developed LiM early (<6 months (LiM<6)) and the 13 patients who developed LiM later (>6 months (LiM>6)) (Extended Data Fig. 1b and Extended Data Table 1). Indeed, as noted above, compared to NED, LiM>6 livers expressed several genes highly enriched in pathways involved in proliferation and liver regeneration (such as 'E2F targets',

'MYC targets', 'PI3K-AKT-MTOR' and 'G2M signaling') (Supplementary Table 7 and Supplementary_Tables_1.xlsx)[6–8]. These pathways were also enriched in EHM versus NED, although to a lesser extent compared to LiM>6 (Supplementary Table 6), therefore demonstrating partial overlap among EHM and LiM>6. Immunostaining for Ki-67 confirmed increased numbers of proliferating cells in EHM and LiM>6 livers (Fig. 2f). In contrast, patients with LiM<6 had no significant GSEA differences compared to NED, and neither were they enriched for the EHM genes, suggesting lack of activation of 'resistance gene programs' in LiM<6 livers. Uniquely, expression of *SORT1*, which encodes for the lysosomal trafficking protein sortilin-1 and is implicated in hepatic cholesterol catabolism and regulation of cytokine secretion in myeloid cells, neutrophils and T cells[9,10], was significantly upregulated in LiM<6 compared to the other recurrence groups (Fig. 2g). Among patients with PaC, high *SORT1* expression was associated with shorter time to LiM (TTLiM), reflecting an approximately three-fold increased risk of early LiM (hazard ratio (HR): 2.96 (95% confidence interval (CI): 1.14–7.84); $P = 0.029$; Fig. 2h).

In summary, inflammatory and proliferative alterations detected at the molecular level distinguish the PaC pre-metastatic liver. Furthermore, the livers of patients with PaC that 'resist' metastatic colonization (for example, EHM and LiM>6) are characterized by distinct transcriptional programs involving interferon signaling, monocyte chemotaxis and proliferation, whereas patients with impending LiM (LiM<6) feature upregulation of *SORT1*.
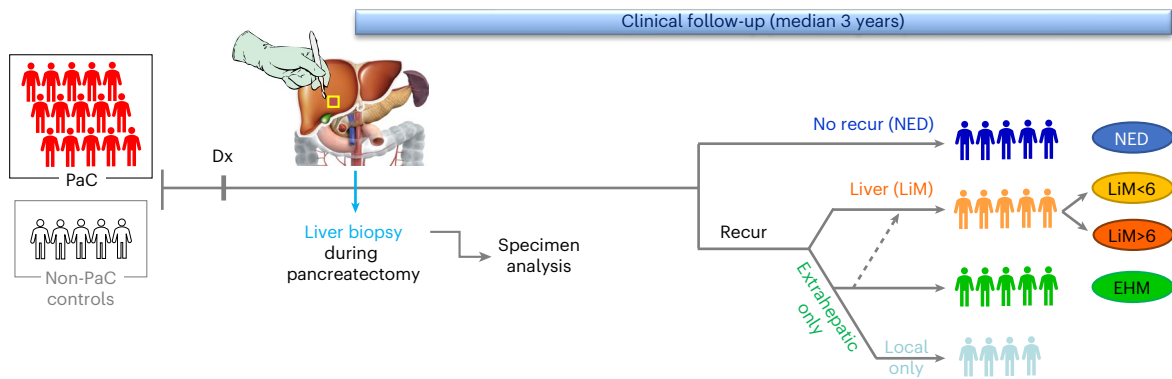
Immune determinants of the hepatic pre-metastatic niche

Although standard histopathological analyses of inflammation, fibrosis or steatosis[11] did not reveal any major differences between PaC and non-PaC livers (Extended Data Fig. 2), we examined individual immune cell types to evaluate their roles in evolution of the hepatic pre-metastatic niche. We previously showed that PaC-derived exosomes are taken up by hepatic Kupffer cells and contribute to the recruitment of bone-marrow-derived cells (BMDCs) to promote LiM[12]. Thus, we stained liver tissue with the myeloid/BMDC marker CD11B, the macrophage marker CD68 and the myeloid activation marker IBA-1. Consistently, patients with PaC had significantly higher numbers of liver-infiltrating CD11B+ cells compared to non-PaC patients (Fig. 3a).

Although we did not observe differences in the total numbers of CD68+ or IBA-1+ macrophages (Extended Data Fig. 3a,b) between PaC and non-PaC livers, blinded examination by a pathologist observed altered spatial organization with moderate or strong IBA-1+ staining in portal tracts in 68% of patients with PaC compared to only 11% of non-PaC patients ($P = 0.001$; Fig. 3b). Additionally, nearly 40% of patients with PaC had either focal or diffuse aggregates of IBA-1+ cells in the liver parenchyma, outside the portal areas, versus only 11% of patients in the non-PaC group exhibiting only focal aggregates ($P = 0.005$; Fig. 3c).

Interestingly, co-staining of these three myeloid markers showed a great degree of overlap of CD68 and IBA-1 but less than 25% overlap of these markers with CD11B (Extended Data Fig. 3c), suggesting that other cells contribute to the liver-infiltrating CD11B+ cell pool. We, thus, expanded our analysis to neutrophils, which have been shown to contribute to LiM in animal models[13,14]. We found prominent clusters of neutrophils, which formed neutrophil extracellular traps (NETs), represented by neutrophil elastase (NE) and citrullinated histone H3 positivity (Ct-H3) ($P = 0.016$ and $P = 0.006$, respectively; Fig. 3d) in PaC versus non-PaC livers. Furthermore, we examined putative anti-tumor effector cells and observed significantly higher numbers of CD3+ lymphocytes in pre-metastatic livers of PaC compared to non-PaC patients ($P = 0.008$; Fig. 3e) and confirmed by semiquantitative scoring by a blinded pathologist ($P = 0.028$; Fig. 3f). Sub-analysis of CD3+ lymphocyte subsets did not reveal significant differences in CD8+ or CD8− cells between PaC and non-PaC (Extended Data Fig. 3d–f).

Schema of specimen collection and patient follow-up

Types of comparisons included in the study

Comparison		Included patients	Remarks
	PaC vs non-PaC	All	Patients with inadequate material for the specific analyses were excluded from those.
	Recurrence patterns	PaC patients, except those with early death and unclear recurrence status. Patients with isolated local recurrence were excluded.	Comparison of individual cellular, molecular and metabolic features (e.g., CD3⁺ cell infiltration). In certain cases, recurrence patterns were combined, e.g. NED vs {EHM + LiM>6 + LiM<6} to analyze NED vs any distant recurrence, etc.
	Time to Liver metastasis	PaC patients, except those with early death and unclear recurrence status	PaC patients classified according to presence or absence of LiM. Time to LiM was analyzed by Kaplan–Meier.

Fig. 1 | Study schema and classification into recurrence groups. Patients with resectable PaC ($n = 49$) who underwent upfront resection were subjected to intraoperative liver biopsy following diagnosis (Dx). Specimens were analyzed postoperatively, and patients were followed thereafter to assess for timing and pattern of recurrence (median follow-up: 36 months). Patients were classified into four recurrence groups: early (<6 months after resection) or late (>6 months after resection) LiM, distant EHM and NED. Patients with isolated local recurrence ($n = 5$) were classified separately and excluded from comparisons of individual recurrence groups, as described in the manuscript and summarized in the table above. Patients with benign or pre-malignant (peri-)pancreatic lesions undergoing pancreatectomy were recruited as controls and underwent similar specimen collection and analysis (non-PaC; $n = 19$).

Dysfunctional immune effector cells in pre-metastatic livers

To further characterize the immune infiltrates of pre-metastatic livers, we performed single-cell RNA sequencing (scRNA-seq) on hepatic immune cells isolated from three non-PaC and five PaC patients (Supplementary Table 8 and Extended Data Fig. 4). Driver and marker genes for each cluster (Extended Data Fig. 4b,c) were concordant with previous scRNA-seq studies[15,16]. Our analysis demonstrated higher proportions of T cells in PaC livers ($P = 0.016$; Fig. 3g), consistent with the aforementioned immunostaining data (Fig. 3e,f). The natural killer (NK) T cell fraction (which may also include other innate lymphocytes) was significantly decreased in the PaC group ($P = 0.033$). Notably, PaC intrahepatic T cells had altered expression patterns of activation/exhaustion genes, such as upregulation of the co-stimulatory molecules *CD27* and *CD97* and the co-inhibitory receptor *KLRG1* and downregulation of effector genes, such as *IFNG* and *GNLY* (Supplementary Table 9), similar to a previous report on hepatocellular carcinoma-infiltrating T cells[15]. Furthermore, PaC T cells had upregulated *CXCR4*, which has been associated with exclusion from tumor entry[17], and downregulated *XCL1* and *XCL2*, which are involved in cross-activation of dendritic cells (DCs)[18,19].

ITGAM/CD11B, the immune cell marker most strikingly enriched in PaC livers by immunostaining (Fig. 3a), was predominantly expressed in the myeloid subpopulation as well as in the NK cell cluster, with little overlap with the macrophage marker CD68 (Extended Data Fig. 4d). Conversely, NK cells were significantly enriched within CD11B⁺ cells in PaC livers ($P = 0.008$; Fig. 3h), whereas CD14⁺ and CD16⁺ monocytes were decreased. CD11B⁺ NK cells in PaC livers had increased expression of genes involved in NK cell cytotoxicity and interaction with non-lymphoid cell types via killer cell lectin-like receptors, such as *GZMB*, *PRF1* and *KLRD1*, compared to non-PaC livers

(Extended Data Fig. 5a,b). However, PaC livers exhibited decreased expression of *IFNG* and *TNF*, suggesting an impaired ability to recruit and activate T cells[20,21].

To understand the composition of the CD3⁺ population, we performed subset analysis of scRNA-seq exclusively on CD3-expressing cells[22] (Fig. 3i and Extended Data Fig. 5c–e). Despite a trend for increase in mucosa-associated invariant T (MAIT) cells among patients with PaC ($P = 0.109$), relative abundances of T cell subsets and NKT cells were not significantly altered (Extended Data Fig. 5e). Using the CIBERSORT methodology[23], we deconvoluted the bulk liver tissue transcriptomic data in the larger patient cohort and confirmed the increase in activated NK cells in PaC both with the original CIBERSORT cell signatures (Extended Data Fig. 5f) as well as with our T/NKT cell signature (Extended Data Fig. 5g).
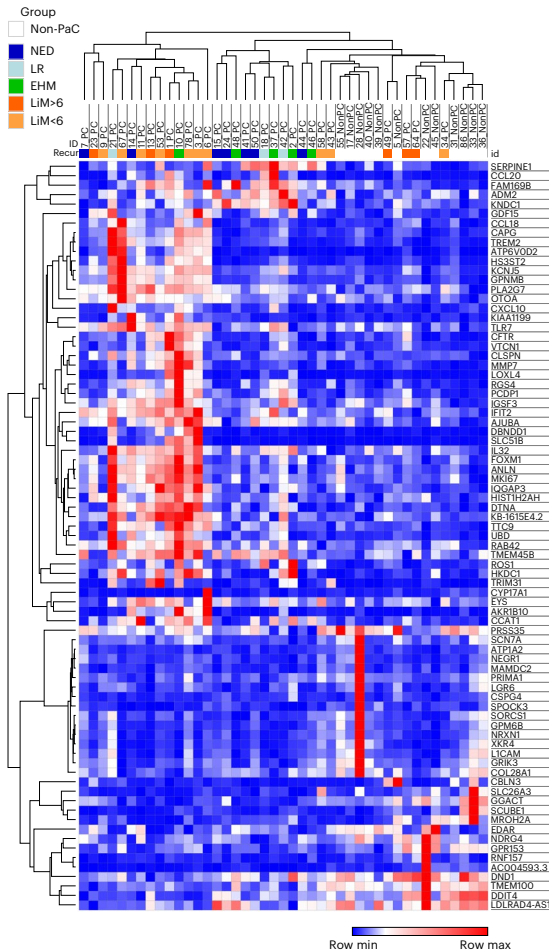
We further confirmed the abundance and spatial distribution of hepatic CD3⁺ cells by analyzing CD4⁺, CD8⁺, NKT/γδT (NKG2A and TCRγδ) and regulatory T (Treg; FOXP3⁺) cells using imaging mass cytometry (Extended Data Fig. 6). Although an increase in CD3⁺ cells was confirmed, the cellular distribution or individual cell types did not reach statistical significance in this subcohort, although a trend for increased total CD8⁺ and CD4⁺ cells in PaC recapitulated our immunofluorescence data (Fig. 3e,f and Extended Data Fig. 3d–f).

Taken together, these data indicate the presence of a unique immune cell landscape in the liver pre-metastatic niche.
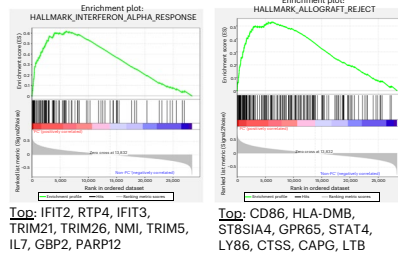
Hepatic immune cells predict distinct recurrence patterns

Next, we assessed the impact of various immune cell features on PaC recurrence patterns (Fig. 4 and Extended Data Fig. 7). Consistent with our gene expression analysis showing augmented inflammation in
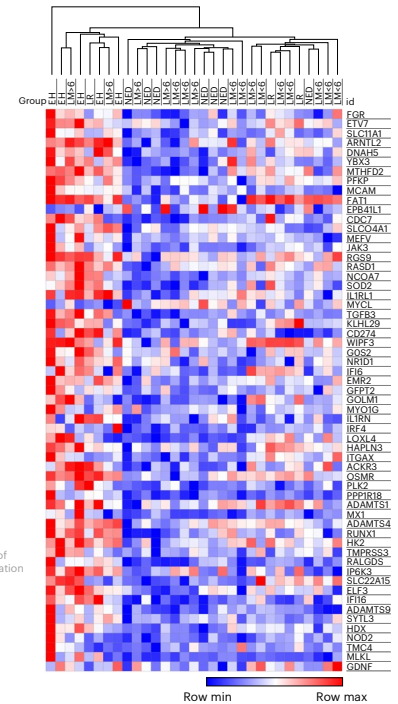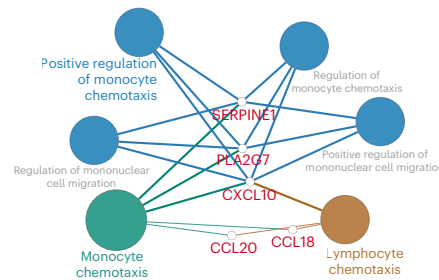
a PaC vs non-PaC: liver mRNA-seq
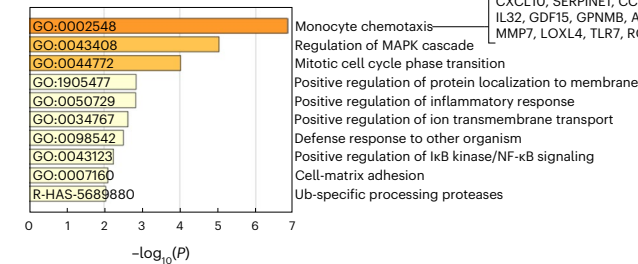
b GSEA, pathways up in PaC (vs non-PaC)

Top: IFIT2, RTP4, IFIT3, TRIM21, TRIM26, NMI, TRIM5, IL7, GBP2, PARP12

Top: CD86, HLA-DMB, ST8SIA4, GPR65, STAT4, LY86, CTSS, CAPG, LTB

c PaC vs non-PaC: Immune cell gene clustering

e 'EHM vs NED' signature

d PaC vs non-PaC: GO pathway analysis

CXCL10, SERPINE1, CCL18, CCL20, PLA2G7, IL32, GDF15, GPNMB, ADM2, TREM2, CEMIP, MMP7, LOXL4, TLR7, RGS4, AKR1B10

GO term	pathway
GO:0002548	Monocyte chemotaxis
GO:0043408	Regulation of MAPK cascade
GO:0044772	Mitotic cell cycle phase transition
GO:1905477	Positive regulation of protein localization to membrane
GO:0050729	Positive regulation of inflammatory response
GO:0034767	Positive regulation of ion transmembrane transport
GO:0098542	Defense response to other organism
GO:0043123	Positive regulation of IκB kinase/NF-κB signaling
GO:0007160	Cell-matrix adhesion
R-HAS-5689880	Ub-specific processing proteases

$-\log_{10}(P)$

f Liver Ki-67$^+$ cells

g *SORT1* gene expression

$P = 0.005$
$P = 0.199$
$P = 0.028$

h *SORT1*: time-to-LiM

log-rank $P = 0.022$

SORT1 mRNA above median (403)

Low ($n = 16$)
High ($n = 16$)
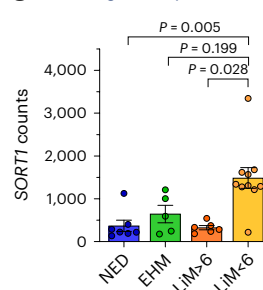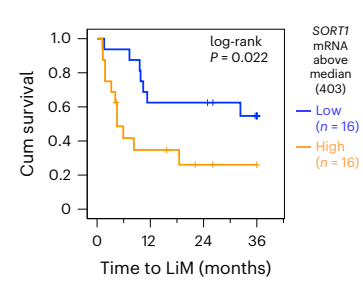
Fig. 2 | Livers of patients with localized PaC exhibit molecular alterations with prognostic significance. a, mRNA-seq of liver tissue collected intraoperatively identified 79 genes differentially expressed between PaC ($n = 31$) and non-PaC ($n = 12$) patients (Wald test performed using the DESeq2 package with adjustment for multiple comparisons; genes shown were altered >2-fold, with adjusted $P < 0.1$). Patients with PaC were classified into five mutually exclusive recurrence groups: NED; isolated local recurrence (LR); EHM; early liver metastasis (within 6 months, LiM<6); and late LiM (beyond 6 months, LiM>6). **b**, Enriched gene sets related to immune response in PaC livers by GSEA using the Hallmarks of Cancer reference gene set (MSigDB, H; pathways were considered significant if $P < 0.05$, FDR < 0.25). The top 10 genes driving each gene set are listed, in descending order. **c**, Immune cell gene clustering and visualization of genes significantly upregulated in PaC livers by Cytoscape ClueGO. **d**, Pathway gene expression analysis of significantly upregulated genes by Metascape (cutoff $P < 0.1$, after adjustment for multiple comparisons). **e**, Unsupervised clustering using the genes differentially expressed between patients with EHM and patients with NED. **f**, Confirmatory Ki-67 immunostaining showing upregulation in recurrence groups ($n = 38$; mean ± s.e.m.; Kruskal–Wallis ANOVA $P = 0.023$, pairwise testing with correction for multiple comparisons shown if $P < 0.25$). **g,h**, *SORT1* expression in recurrence groups, showing upregulation in LiM<6 ($n = 29$; mean ± s.e.m.; Kruskal–Wallis ANOVA $P = 0.002$, pairwise testing with correction for multiple comparisons shown if $P < 0.25$) (**g**) and association with time to LiM (TTLiM) ($n = 32$; log-rank test; $P = 0.022$) (**h**). GO, Gene Ontology.
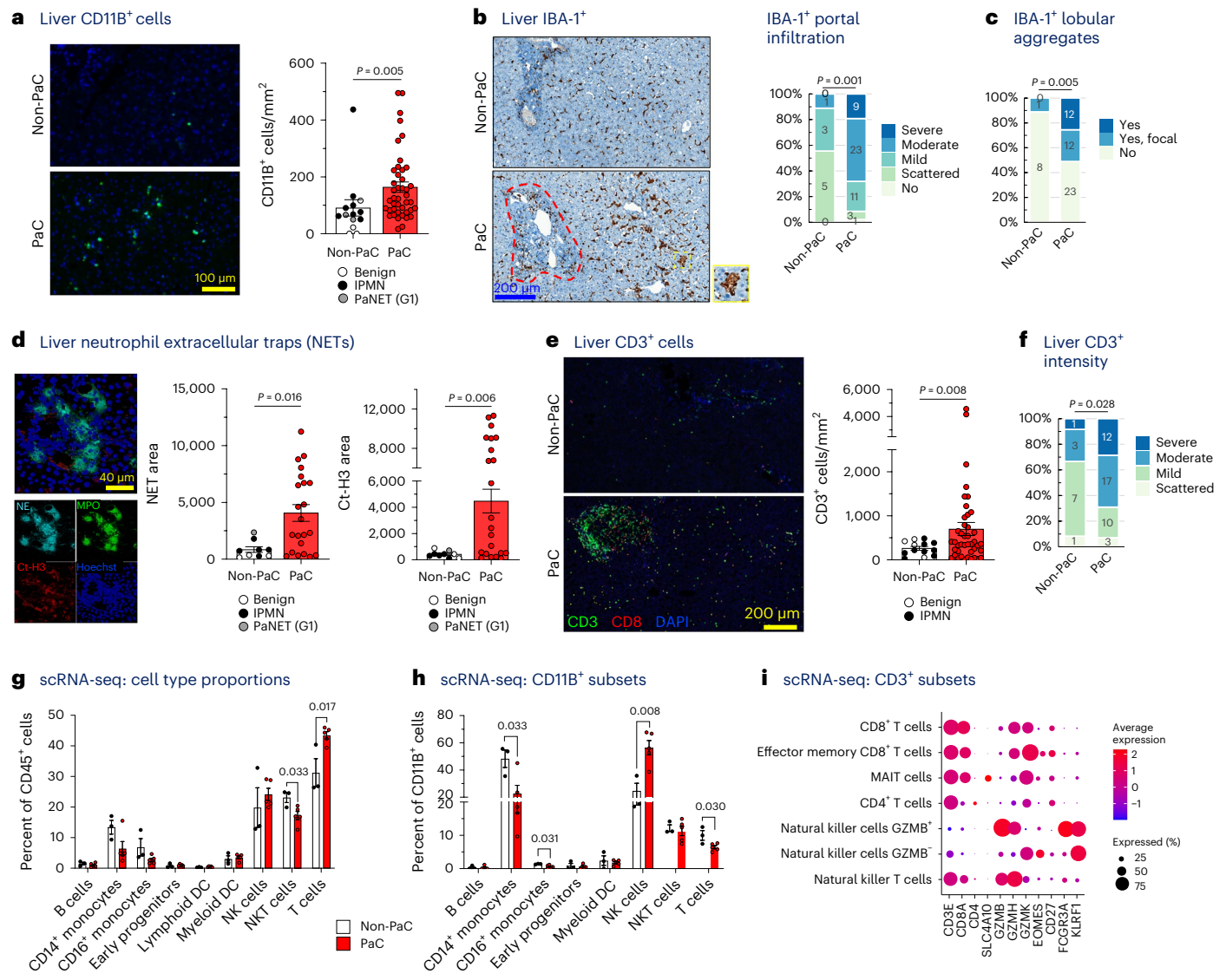
Fig. 3 | Pre-metastatic livers of patients with PaC feature changes in infiltrating immune cells. a, Liver biopsies were stained by IF for the myeloid marker CD11B, quantified with ImageJ and compared between PaC ($n = 44$) and non-PaC ($n = 14$) (Mann–Whitney U-test; $P = 0.005$). **b,c**, Liver biopsies were stained by IHC for the macrophage activation marker IBA-1 and compared between PaC ($n = 47$) and non-PaC ($n = 9$) after manual quantification by a blinded pathologist of the extent of IBA-1+ cell infiltration in the portal tracts (red outline; Somers' d; $P = 0.001$) (**b**) and the presence of IBA-1+ cell aggregates (yellow outline) in the lobular portions of the liver parenchyma (Somers' d; $P = 0.005$) (**c**). **d**, Liver biopsies were stained for NE and Ct-H3 to identify clusters consistent with NETs. Stained area was quantified with ImageJ and compared between PaC ($n = 22$) and non-PaC ($n = 9$) (Mann–Whitney U-test: NE area, $P = 0.016$; Ct-H3 area, $P = 0.006$). **e,f**, Liver biopsies were co-stained by IF for CD3 and CD8. **e**, CD3+ T

cells were quantified using ImageJ and compared between PaC ($n = 42$) and non-PaC ($n = 13$) (t-test; $P = 0.008$). **f**, A blinded pathologist quantified the intensity of CD3+ lymphocyte staining (Somers' d; $P = 0.028$). **g–i**, scRNA-seq was performed on hepatic NPCs (>90% CD45+) from three non-PaC and five PaC patients and analyzed as shown in Extended Data Figs. 4 and 5. **g**, Comparison of the relative abundance of the major cell clusters between PaC and non-PaC (multiple t-tests with correction for multiple comparisons, shown if $P < 0.25$). **g**, The percentage of different cell clusters among CD11B+ cells was calculated and compared between PaC and non-PaC (multiple t-tests with correction for multiple comparisons, shown if $P < 0.25$). **h**, Subset analysis of CD3+ cells (Extended Data Fig. 4) resulted in four T cell subclusters as well as NKT cells and two NK cell clusters (MAIT cells). **i**, Subset analysis of CD3+ cells resulted in four T cell subclusters as well as NKT cells and two NK cell clusters (MAIT cells). Mean ± s.e.m. is shown in bar graphs.

patients who developed metastases, significant portal inflammation was observed in patients with subsequent distant metastasis compared to the NED group ($P = 0.031$; Fig. 4a). Both portal and lobular inflammation were most intense in the EHM group, followed by the LiM>6 group (Fig. 4a and Extended Data Fig. 7a). Strikingly, analysis of neutrophils in the metastatic subgroups showed notably increased NETs in LiM<6 compared to the other recurrence groups ($P < 0.001$; Fig. 4b). Despite a lower overall level of other inflammatory readouts, increased NETs may play an immunosuppressive role, as shown in preclinical studies[24]. No other differences in myeloid cells, compared by CD11B+, IBA1+ and CD68+

cell density, were observed (Extended Data Fig. 7b–e). The hepatic parenchymal distribution of CD3+ lymphocytes was significantly different between patients with and without LiM ($P = 0.016$; Fig. 4c), whereas no significant differences in absolute counts of CD3+ and CD8+ lymphocytes were noted (Extended Data Fig. 7f–h). Notably, the EHM group had mostly widespread lobular infiltration, whereas the LiM<6 group had predominantly scattered to few lobular CD3+ lymphocytes.

These observations suggest that the exact composition of the enhanced immune infiltrate in PaC pre-metastatic livers may be a critical determinant of the metastatic outcome. Notably, our data
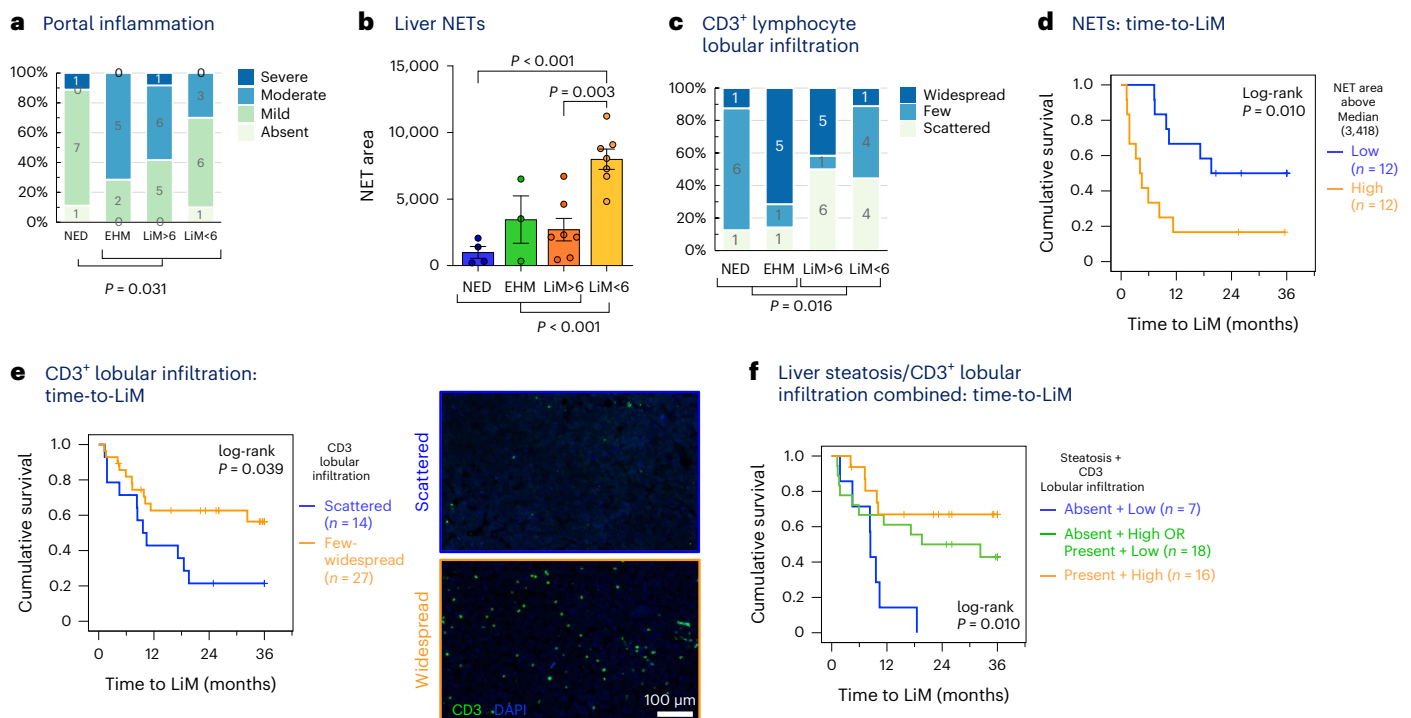
Fig. 4 | Alterations in pre-metastatic liver-infiltrating immune cells correlate with patterns and timing of metastasis. a, Liver biopsies obtained at the time of resection from patients with NED or distant recurrence (EHM, LiM>6 or LiM<6) were manually scored by a blinded pathologist for portal inflammation (Kruskal–Wallis test). **b**, NET area quantified as in Fig. 3d was compared among the different recurrence groups (*n* = 21; mean ± s.e.m.; ANOVA *P* = 0.001; multiple *t*-tests with correction for multiple comparisons, shown if *P* < 0.25). **c**, Liver CD3+ lymphocyte lobular infiltration was manually scored by a blinded pathologist and compared among the different recurrence groups as well as between LiM and no LiM (Kruskal–Wallis test; *P* = 0.016). **d**, Kaplan–Meier curve of time to LiM for high versus low NET area, as quantified in **b** (*n* = 24; log-rank test; *P* = 0.010). **e**, Kaplan–Meier curve of time to LiM for scattered versus few/widespread lobular CD3+ lymphocyte lobular infiltration, as scored in **c**, with representative examples shown in side panels (log-rank test; *P* = 0.039). **f**, Steatosis (absence versus presence) and CD3+ lymphocyte lobular infiltration (as in **c**) were used to classify patients with PaC in three subgroups, and TTLiM was compared among them (*n* = 42; log-rank test; *P* = 0.010). inf., infiltration.

indicate that high NET burden and low CD3+ lymphocyte lobular infiltration could have important prognostic value in estimating the risk of metastasis and, in particular, early LiM, which is further corroborated by the association of these immune cell alterations with shorter TTLiM (*P* = 0.025 and *P* = 0.039 (log-rank), respectively; Fig. 4d,e).

Furthermore, we hypothesized that the metabolic status of the liver could influence immune infiltration and serve as another predictor of recurrence patterns. Histologically graded steatosis (Extended Data Fig. 2) was significantly more prominent in patients with recurrence outside the liver compared to LiM (*P* = 0.034; Extended Data Fig. 8a). Although presence of steatosis did not significantly correlate with TTLiM (Extended Data Fig. 8b), an important interaction with lobular CD3+ cell infiltration was observed (Fig. 4f). Specifically, patients with steatosis and prominent CD3+ lobular infiltration had a significantly lower incidence of LiM, whereas absence of steatosis and concurrent lack of CD3+ lobular infiltration distinguished a subgroup of patients all of whom developed LiM within 1.5 years (*P* = 0.010; Fig. 4f). In conclusion, hepatic steatosis, together with prominent CD3+ lobular infiltration, represents an immunometabolic phenotype potentially counteracting LiM.

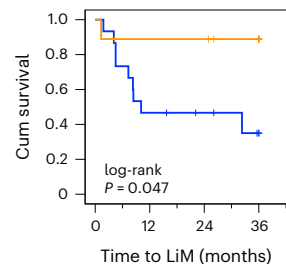## Metabolic reprogramming in pre-metastatic livers predicts LiM

To specifically assess metabolic changes within the liver pre-metastatic niche, we performed metabolomic profiling of liver biopsies. Remarkably, PaC livers had significantly decreased creatine and creatinine levels compared to non-PaC livers (*P* < 0.005; Fig. 5a and Extended Data Fig. 8c,d). The observed metabolic changes were likely restricted to the

liver as pre-operative serum creatinine levels did not differ between the two groups (Extended Data Fig. 8e). We also observed significantly enriched arginine and proline metabolism in PaC compared to non-PaC livers (>8-fold, *P* < 0.05; Fig. 5b and Extended Data Fig. 8c,d). Levels of carbamoyl-phosphate, a precursor of citrulline, were significantly higher in PaC (*P* = 0.013), suggesting a potential diversion of the pathway toward augmented utilization of citrulline (Fig. 5c). In support of this finding, Ct-H3 correlated inversely with hepatic creatine levels (Spearman's *r* = −0.6, *P* = 0.031; Fig. 5d).
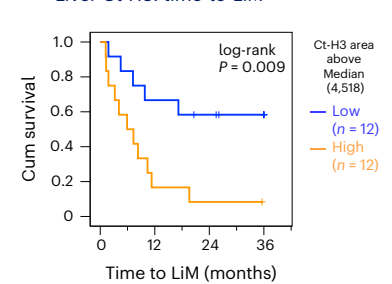
According to hierarchical clustering analysis, a panel of 15 metabolites distinguished most of the patients who subsequently developed LiM from the patients with EHM and the patients with NED (Extended Data Fig. 8f). Consistently, low hepatic creatine levels were associated with shorter TTLiM (*P* = 0.047; Fig. 5e) and were lowest in patients with LiM>6 (Extended Data Fig. 8g). Furthermore, patients who eventually developed LiM had significantly higher Ct-H3 immunostaining that was not limited to immune cells (*P* = 0.004; Fig. 5f), with high Ct-H3 correlating with earlier LiM (log-rank *P* = 0.009; Fig. 5g). Taken together, arginine metabolism and urea cycle are dysregulated in pre-metastatic livers, and specific metabolites, including creatine and Ct-H3, show promise as prognostic indicators for LiM in patients with PaC.

Machine learning predictive modeling for metastatic patterns

We hypothesized that combining pre-metastatic liver-specific signatures could more accurately inform the risk for LiM in PaC. We employed the aforementioned individually significant histopathological (Figs. 3 and 4) and metabolomic (Fig. 5) variables, as well as *SORT1* and the

a PaC vs non-PaC: Liver metabolomics

b PaC vs non-PaC: metabolite set enrichment analysis
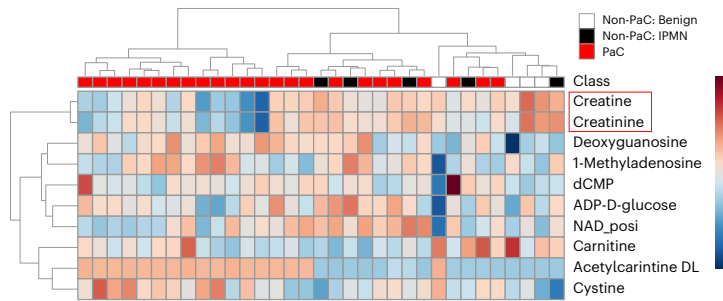
c
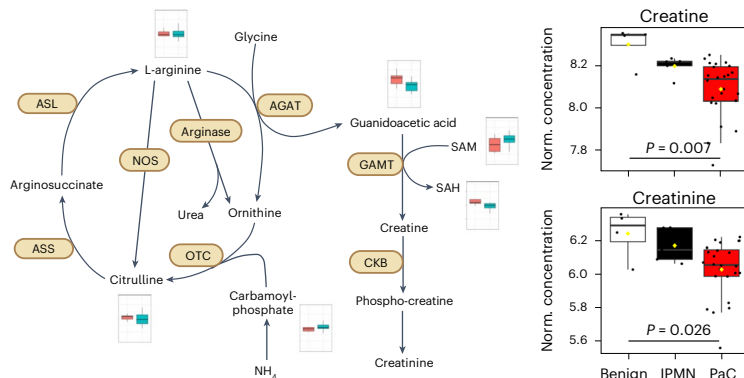
d Liver creatine –Ct-H3 correlation
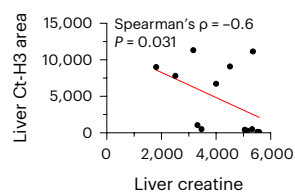
e Liver creatine: time-to-LiM

f Liver Ct-H3

g Liver Ct-H3: time-to-LiM
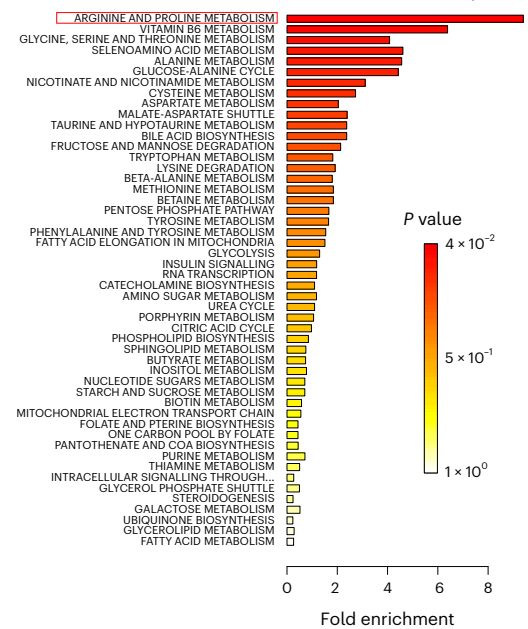
Fig. 5 | Metabolic features of the pre-metastatic liver correlate with patterns of recurrence in PaC. a–c, Metabolomic analysis of liver biopsies in 24 PaC versus nine non-PaC patients revealed creatine and creatinine to be most prominently differentially expressed using supervised clustering ($P < 0.001$, FDR < 0.15 and $P < 0.005$, FDR < 0.2, respectively) (**a**) and enriched arginine and proline metabolism in PaC livers by metabolite set enrichment analysis (MSEA) using MetaboAnalyst (**b**). **c**, Schematic showing the metabolism of arginine, citrulline, creatine and creatinine, with the levels of metabolites compared between PaC (teal bars) and non-PaC (light red bars). The levels of hepatic creatine and creatinine were compared between PaC ($n = 24$) and non-PaC ($n = 9$
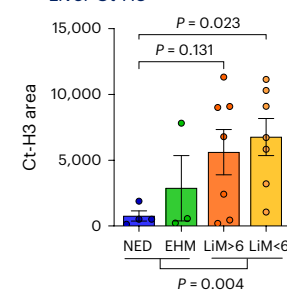
(four benign and five IPMN); box plots represent median ± IQR, with whiskers at 95th percentiles; ANOVA $P = 0.007$ and $P = 0.026$, respectively). **d**, Negative correlation between liver creatine measured in metabolomic analysis and Ct-H3 quantified in Fig. 2e (Ct-H3; $\rho = -0.6$, $P = 0.031$). **e**, Kaplan–Meier curve of TTLiM for patients with high versus low creatine levels (based on median; $n = 24$; log-rank $P = 0.047$). **f,g**, Total liver Ct-H3 differed among recurrence groups ($n = 21$; mean ± s.e.m.; ANOVA $P = 0.023$; multiple t-tests with correction for multiple comparisons, shown if $P < 0.25$) (**f**) and associated with shorter TTLiM by Kaplan–Meier analysis ($n = 24$; log-rank $P = 0.009$) (**g**). IQR, interquartile range.

defining genes of the EHM transcriptomic signature (Fig. 2), and used a machine-learning-based approach (MLA) to create a predictive model for metastatic outcome. Body mass index (BMI) and biliary obstruction were included as variables because these could influence or confound cellular and molecular features of the liver but did not contribute to the final models (Supplementary Table 10). We generated four separate models that predicted the different metastatic outcomes in a binary fashion: LiM, early LiM (LiM<6), EHM and NED (Fig. 6a). The four models performed well, with areas under the receiver operating characteristic curves (AUCs) of 0.83–0.89. The early LiM model, which included three features (*SORT1*, *NR1D1* and NET area), had the best performance, with 90% sensitivity, 87% specificity and an AUC of 0.87.

We combined the predicted outcomes to classify patients into the recurrence patterns of interest (Fig. 6b). Patients were assigned to the metastatic group of the model that gave the highest risk score

(Fig. 6c and Supplementary Table 11). The combined model performed well for identification of early LiM, with 90% accuracy (Fig. 6d). Of the 10 patients who developed early LiM, nine were classified correctly. Conversely, nine of 12 patients predicted to develop early LiM were correctly classified. The overall accuracy of the combined model in assigning patients to specific recurrence groups was 78%.

In summary, our findings demonstrate the potential to predict PaC recurrence patterns via immunometabolic characterization of peri-operative liver biopsies (summarized in Fig. 6e) which is particularly accurate in predicting early LiM.

Discussion

PaC is one of the most challenging malignancies due to its protracted subclinical course and early LiM, which almost universally results in a fatal outcome. We reported previously that only 34% of resected patients

with PaC remain alive 1 year after diagnosis of LiM[2]. Thus, reliable strategies for identification of patients at high risk of distant recurrence in the pre-operative setting are urgently needed. Our multi-omics approach that comprehensively characterizes the liver pre-metastatic niche in patients with PaC demonstrates potential for such prognostic implementation.

Based on preclinical studies[12–14,25,26], we hypothesized that metastatic sites, particularly the liver, exhibit detectable microenvironmental changes before clinical evidence of metastasis. Alterations in resident cell phenotypes, extracellular matrix (ECM) and immune cell infiltration collectively create a pre-metastatic niche[27,28]. Using transcriptomics, metabolomics and histopathology, we observed that pre-metastatic livers of patients with PaC indeed displayed a prominent inflammatory response with augmented myeloid and lymphoid cell subsets at the time of resection. At the mRNA level, the inflammatory signature was prominent in patients with PaC who primarily developed EHM and secondarily late LiM as compared to long-term survivors. This suggests that the EHM-specific transcriptomic signature may represent a defensive anti-tumor immune response within the liver.

Although PaC livers had increased CD11B^{+} cell infiltration and a higher number of activated NK cells compared to non-PaC livers, the levels of intrahepatic CD11B^{+} cells did not differ significantly among patients with PaC with varying metastatic patterns. By contrast, CD3^{+} lymphocyte infiltration was elevated in PaC livers, especially in patients who remained free of LiM during follow-up. Analysis of these enriched CD3^{+} lymphocytes by scRNA-seq and imaging mass cytometry did not identify any specific expanded subset, although the strongest trends were observed for CD8^{+} lymphocytes. Furthermore, lobular infiltration of CD3^{+} lymphocytes correlated inversely with TTLiM and, thus, may have prognostic significance. These observations suggest that myeloid cell infiltration in the liver is an early event during PaC metastasis and a hallmark of the liver pre-metastatic niche, whereas T cell infiltration later in PaC progression may reflect anti-tumor activity. Thus, patients who fail to mount an intrahepatic T cell immune response are more likely to develop subsequent LiM. These findings are consistent with a report by Pommier et al.[29], who found that isolated, disseminated PaC cells in mice were kept in check by infiltrating T cells, whereas T cell depletion combined with disseminated tumor cell endoplasmic reticulum stress enabled the development of macro-metastases.

We also observed an increased neutrophil infiltration and NET formation in PaC livers that developed LiM, particulary those that developed LiM within 6 months after resection. Preclinical studies have linked neutrophils and NETs to pre-metastatic niche formation and promotion of metastasis, potentially through inhibition of cytotoxic T cells as well as release of ECM-degrading enzymes that facilitate tumor cell migration and adhesion[13,14]. The precise role of NETs in hepatic metastasis remains to be determined.

In addition, we found several metabolic alterations in the liver of patients with PaC. We observed that patients with subsequent LiM had less microscopic evidence of hepatic steatosis at the time of resection. Previous studies suggested immunomodulatory roles of cholesterol and fatty acid metabolites, which may account for these observations[30]. For example, it was previously shown that lipid-rich hepatic DCs are more immunogenic and can promote lymphocyte-mediated anti-tumor immune responses, whereas lipid-poor DCs are tolerogenic and induce Treg responses with resultant anergy to cancer[31]. Reinforcing these observations, we noted upregulation of *SORT1* gene expression in early LiM, which has pleiotropic functions in hepatic cholesterol metabolism and has been shown to be regulated post-transcriptionally by Toll-like receptor signaling[9,10]. Furthermore, patients with steatosis and concurrent T cell lobular infiltration were least susceptible to LiM development. This particular phenotype is intriguing as it has similarities with the pathogenesis of non-alcoholic steatohepatitis, which features robust Th1, NKT and NK cell responses[31–33]. Thus, it may serve not only as a biomarker but also as a potential therapeutic

target. It should be emphasized that the inverse association between steatosis and LiM does not necessarily imply causation, nor can the timing of the observed events be determined by evaluating one time-point. Does steatosis and CD3^{+} infiltration precede the inception of PaC, or does this evolve during pancreatic carcinogenesis? Our recently published work showed that a subset of tumor-derived extra-cellular particles termed 'exomeres' preferentially home to the liver and increase Kupffer-cell-mediated fat deposition and interfere with drug metabolism[34]. This might support hepatic steatosis and related immune infiltration as an evolving secondary process in a subset of patients with pancreatic carcinogenesis.
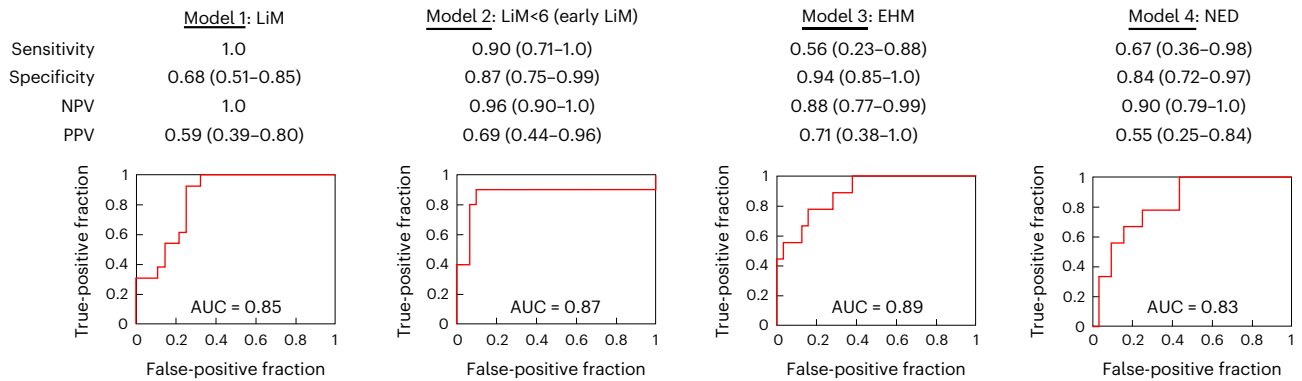
Moreover, we observed that hepatic creatine levels were reduced in patients with PaC and, more significantly, in patients who developed LiM. Creatine serves as an energy source for activated cytotoxic T cells, whereas depletion of T cell creatine leads to an exhausted phenotype[35]. Our metabolomic data suggest that PaC metastatic growth may be linked, at least in part, to immunometabolic deregulation and impaired anti-tumor immune responses. Further studies could precisely delineate the immunometabolic events within the liver pre-metastatic niche and provide a promising therapeutic target to curtail LiM.

The ability to predict which patients will develop metastasis is a critical goal for PaC management. That a portion of patients with seemingly localized PaC develop LiM within months after resection underscores the need for predictive tools to determine the optimal treatment approach. Identifying patients with a high probability of early LiM would provide strong justification to avoid surgical intervention in favor of initial systemic therapy, whereas patients who do not develop metastasis would undergo upfront surgical resection. To this extent, we created a predictive model for early LiM based on findings in peri-operative liver biopsies. Although this approach will require further refinement and validation in larger patient cohorts, our results support the benefit of incorporating pre-metastatic liver biopsy into the pre-operative evaluation of non-metastatic PaC. Patients with a robust anti-tumor inflammatory signature and steatosis may be at lower risk of LiM, whereas patients exhibiting a high frequency of NETs and upregulated *SORT1* in pre-metastatic livers may be at higher risk for rapid metastasis.
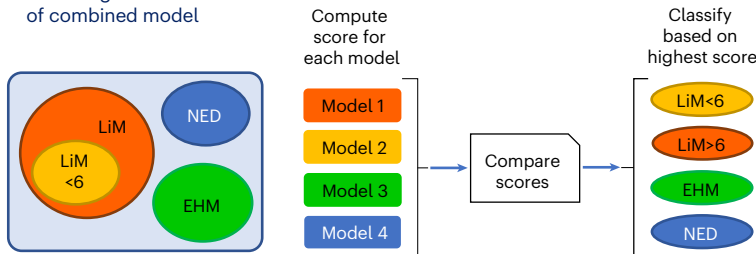
Currently, there is no reliable method to predict metastatic propensity of PaC, except for a markedly elevated serum CA19-9. However, high CA19-9 may result from large primary tumors rather than metastasis, and it does not inform on the timing and patterns of recurrence. Moreover, patients without elevated CA19-9 are still at risk for metastasis. A biomarker that predicts PaC organotropism and recurrence timing could have direct implications in therapeutic decision-making. In our defined PaC recurrence groups, for example, a patient predicted to develop early LiM could be managed with total NAT and maximum chemotherapy upfront (for example, 12 cycles of mFOLFIRINOX) before considering resection. Patients predicted to have late LiM could be treated with standard dose NAT. On the other hand, patients with EHM, who exhibited the strongest anti-metastatic features, may be better suited for approaches that can enhance anti-tumor immune responses, such as neoadjuvant chemoradiation with or without immune check-point inhibitors. Furthermore, knowledge of the expected recurrence group could dictate frequency of post-resection surveillance, with patients predicted to develop early LiM being monitored most frequently (for example, every 2 months initially) and less frequently for patients predicted as NED.

Our predictive (as opposed to prognostic) analysis of the pre-metastatic liver profile could have implications for selecting the best treatment modality for patients with borderline resectable and locally advanced PaC and may even have repercussions for the selection of the best candidates for cytoreduction of liver oligometastatic disease. Currently, the overwhelming majority of patients with PaC with resectable liver-confined metastases are managed with systemic therapy in a palliative setting, whereas only a very limited number of

a Recurrence pattern binary prediction models

	Model 1: LiM	Model 2: LiM<6 (early LiM)	Model 3: EHM	Model 4: NED
Sensitivity	1.0	0.90 (0.71–1.0)	0.56 (0.23–0.88)	0.67 (0.36–0.98)
Specificity	0.68 (0.51–0.85)	0.87 (0.75–0.99)	0.94 (0.85–1.0)	0.84 (0.72–0.97)
NPV	1.0	0.96 (0.90–1.0)	0.88 (0.77–0.99)	0.90 (0.79–1.0)
PPV	0.59 (0.39–0.80)	0.69 (0.44–0.96)	0.71 (0.38–1.0)	0.55 (0.25–0.84)

AUC = 0.85   AUC = 0.87   AUC = 0.89   AUC = 0.83

(ROC plots: True-positive fraction vs False-positive fraction)

b Flow diagram of combined model

Compute score for each model: Model 1, Model 2, Model 3, Model 4 → Compare scores → Classify based on highest score: LiM<6, LiM>6, EHM, NED

c Combined model truth table

n = 41	Actual			
Predicted	NED	EHM	LiM>6	LiM<6
NED	7	0	1	1
EHM	0	6	1	0
LiM>6	1	1	10	0
LiM<6	1	1	1	9

d Performance of combined model

	Sensitivity	Specificity	NPV	PPV	Overall accuracy
Early LiM	0.90 (0.71–1.0)	0.87 (0.75–0.99)	0.69 (0.44–0.94)	0.96 (0.90–1.0)	78%
LiM	0.90 (0.56–1.0)	0.90 (0.74–0.98)	0.75 (0.50–0.90)	0.97 (0.81–1.0)	
EHM	0.77 (0.46–0.95)	0.89 (0.72–0.98)	0.77 (0.52–0.91)	0.89 (0.75–0.96)	
NED	0.77 (0.40–0.97)	0.94 (0.79–0.99)	0.78 (0.46–0.93)	0.94 (0.82–0.98)	

e Summary diagram

Predicated outcome

Pancreatic cancer diagnosis → Pre-operative liver biopsy

↑ NETs 7.6×
↑ Ki-67 2.2×
↓ Creatine 0.76×

YES → • LiM • EHM
↑ Ct-H3 2.2×
↓ Steatosis
↓ Lobular CD3⁺ T cells

YES → • LiM
↑ SORT1 5.3×
↑ Creatine 1.34×
↓ CD45⁺ cells 1.9×
YES → Early LiM
NO → Late LiM

NO → • EHM • NED
↑ MX1 3.3×
↑ NR1D1 2.8×
↑ Ki-67 1.8×
↑ NETs 6.7×
↑ CD11b⁺ NK cells 2.0×
YES → EHM
NO → NED

NO → • NED
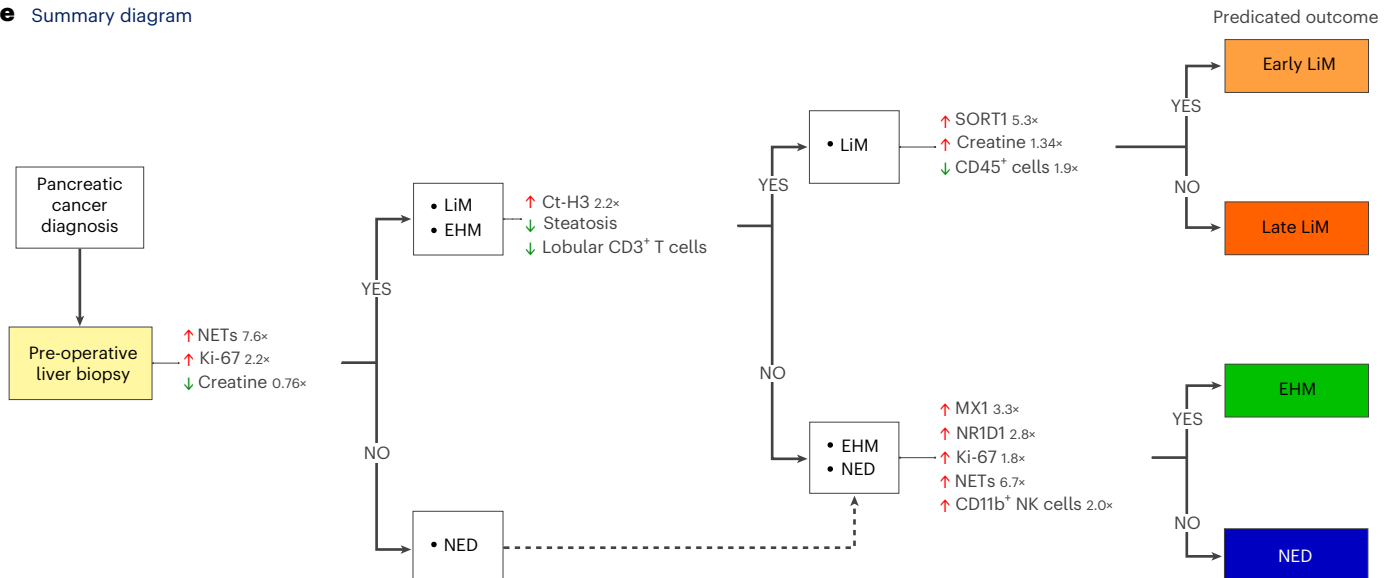
Fig. 6 | Features of the pre-metastatic niche can be used for prediction of future metastasis. Pre-metastatic liver-specific variables were combined in prediction models to classify patients into recurrence patterns. **a**, Performance of four prediction models generated using LOO with 10-fold cross-validation. **b,c**, The four prediction models were run concurrently (**b**), and their output was used to classify patients into recurrence pattern groups (**c**). **d**, Performance of the combined model. **e**, Summary diagram outlining stepwise comparisons of metastatic patterns, with the characteristic molecular, cellular and metabolic features favoring each pattern (fold change is shown for continuous variables). NPV, negative predictive value; PPV, positive predictive value.

such patients are offered metastasectomy, after no progression on prolonged systemic therapy. Knowledge of the status of the unaffected liver (pre-metastatic versus anti-metastatic) could predict the risk of disease progression due to immune evasion and inadequate tumor control and, thus, aid the selection of patients appropriate for cytore-duction, in a similar manner as in colorectal cancer.

A relative weakness of our study is the fact that patients did not have surveillance imaging studies at strictly defined time intervals, which may have affected the assessment of timing of recurrence. For example, one patient (PT16) who was incorrectly predicted to be early LiM (LiM<6) developed clinically detectable LiM at 8.4 months. Also, although biliary obstruction was more prevalent among patients with PaC, and we observed a trend to lower rates of biliary obstruction among patients with PaC who remained recurrence free, we previously reported that biliary obstruction itself does not translate into increased risk of LiM[2]. Lastly, the relatively small sample size in the different recurrence groups may have led to inadequate power to detect true differences and contribute to overfitting of the machine learning model, despite our attempts to minimize it using cross-validation techniques[36].

Nonetheless, strengths of the present study include its prospective design and blinded specimen processing workflow. The downstream multi-parametric analyses were performed before knowledge of patients' recurrence status. Moreover, the fact that patients were enrolled before administration of radiation or systemic therapy eliminated any effects of treatment on the identified liver signatures and demonstrates the potential utility of pre-operative liver biopsies at the time of initial diagnostic workup.

As neoadjuvant treatment of PaC is used with increasing frequency, the effect on the pre-metastatic liver and development of subsequent metastasis warrants investigation to define more effective anti-metastatic regimen for patients. Our data show that the use of multi-model data integration with machine learning may be effective in developing models to predict patients who are likely to fail a surgery-first approach and guide more precise oncologic management.

In conclusion, we present data supporting an overall augmentation of the immune infiltrate and inflammatory response in pre-metastatic PaC livers, with NET-forming neutrophils preceding emergence of LiM and, conversely, CD3+ lymphocytes acting as critical anti-metastatic effector cells. Metabolic derangements involving the creatine/arginine pathways and potentially impacting citrullination within the liver, as well as hepatic steatosis, represent putative immunometabolic links worthy of further investigation. We propose that a liver biopsy at the time of PaC diagnosis may be an invaluable adjunct to provide prognostic information and guide novel treatment approaches, such as liver-directed immunotherapies and metabolic repurposing, in the pre-metastatic setting.

Online content

Any methods, additional references, Nature Portfolio reporting summaries, source data, extended data, supplementary information, acknowledgements, peer review information; details of author contributions and competing interests; and statements of data and code availability are available at https://doi.org/10.1038/s41591-024-03075-7.

References

1. Siegel, R. L., Miller, K. D., Fuchs, H. E. & Jemal, A. Cancer statistics, 2022. *CA Cancer J. Clin.* **72**, 7–33 (2022).
2. Zambirinis, C. P. et al. Recurrence after resection of pancreatic cancer: can radiomics predict patients at greatest risk of liver metastasis? *Ann. Surg. Oncol.* **29**, 4962–4974 (2022).
3. Wangjam, T. et al. Resected pancreatic ductal adenocarcinomas with recurrence limited in lung have a significantly better prognosis than those with other recurrence patterns. *Oncotarget* **6**, 36903–36910 (2015).
4. Bindea, G. et al. ClueGO: a Cytoscape plug-in to decipher functionally grouped gene ontology and pathway annotation networks. *Bioinformatics* **25**, 1091–1093 (2009).
5. Zhou, Y. et al. Metascape provides a biologist-oriented resource for the analysis of systems-level datasets. *Nat. Commun.* **10**, 1523 (2019).
6. Delgado, I. et al. A role for transcription factor E2F2 in hepatocyte proliferation and timely liver regeneration. *Am. J. Physiol. Gastrointest. Liver Physiol.* **301**, G20–G31 (2011).
7. Iakova, P., Awad, S. S. & Timchenko, N. A. Aging reduces proliferative capacities of liver by switching pathways of C/EBPα growth arrest. *Cell* **113**, 495–506 (2003).
8. Zhang, C., Sun, C., Zhao, Y., Ye, B. & Yu, G. Signaling pathways of liver regeneration: biological mechanisms and implications. *iScience* **27**, 108683 (2024).
9. Gao, A. et al. Implications of sortilin in lipid metabolism and lipid disorder diseases. *DNA Cell Biol.* **36**, 1050–1061 (2017).
10. Yabe-Wada, T. et al. TLR signals posttranscriptionally regulate the cytokine trafficking mediator sortilin. *Sci. Rep.* **6**, 26566 (2016).
11. Goodman, Z. D. Grading and staging systems for inflammation and fibrosis in chronic liver diseases. *J. Hepatol.* **47**, 598–607 (2007).
12. Costa-Silva, B. et al. Pancreatic cancer exosomes initiate pre-metastatic niche formation in the liver. *Nat. Cell Biol.* **17**, 816–826 (2015).
13. Grunwald, B. et al. Pancreatic premalignant lesions secrete tissue inhibitor of metalloproteinases-1, which activates hepatic stellate cells via CD63 signaling to create a premetastatic niche in the liver. *Gastroenterology* **151**, 1011–1024 (2016).
14. Seubert, B. et al. Tissue inhibitor of metalloproteinases (TIMP)-1 creates a premetastatic niche in the liver through SDF-1/CXCR4-dependent neutrophil recruitment in mice. *Hepatology* **61**, 238–248 (2015).
15. Zheng, C. et al. Landscape of infiltrating T cells in liver cancer revealed by single-cell sequencing. *Cell* **169**, 1342–1356 (2017).
16. MacParland, S. A. et al. Single cell RNA sequencing of human liver reveals distinct intrahepatic macrophage populations. *Nat. Commun.* **9**, 4383 (2018).
17. Feig, C. et al. Targeting CXCL12 from FAP-expressing carcinoma-associated fibroblasts synergizes with anti–PD-L1 immunotherapy in pancreatic cancer. *Proc. Natl Acad. Sci. USA* **110**, 20212–20217 (2013).
18. Brewitz, A. et al. CD8+ T cells orchestrate pDC-XCR1+ dendritic cell spatial and functional cooperativity to optimize priming. *Immunity* **46**, 205–219 (2017).
19. Bottcher, J. P. et al. NK cells stimulate recruitment of cDC1 into the tumor microenvironment promoting cancer immune control. *Cell* **172**, 1022–1037 (2018).
20. Mikulak, J., Bruni, E., Oriolo, F., Di Vito, C. & Mavilio, D. Hepatic natural killer cells: organ-specific sentinels of liver immune homeostasis and physiopathology. *Front. Immunol.* **10**, 946 (2019).
21. Krueger, P. D., Lassen, M. G., Qiao, H. & Hahn, Y. S. Regulation of NK cell repertoire and function in the liver. *Crit. Rev. Immunol.* **31**, 43–52 (2011).
22. Dominguez Conde, C. et al. Cross-tissue immune cell analysis reveals tissue-specific features in humans. *Science* **376**, eabl5197 (2022).
23. Newman, A. M. et al. Robust enumeration of cell subsets from tissue expression profiles. *Nat. Methods* **12**, 453–457 (2015).
24. Adrover, J. M., McDowell, S. A. C., He, X. Y., Quail, D. F. & Egeblad, M. NETworking with cancer: the bidirectional interplay between cancer and neutrophil extracellular traps. *Cancer Cell* **41**, 505–526 (2023).
25. Aiello, N. M. et al. Metastatic progression is associated with dynamic changes in the local microenvironment. *Nat. Commun.* **7**, 12819 (2016).

26. Connolly, M. K. et al. Distinct populations of metastases-enabling myeloid cells expand in the liver of mice harboring invasive and preinvasive intra-abdominal tumor. *J. Leukoc. Biol.* **87**, 713–725 (2010).

27. Liu, Y. & Cao, X. Characteristics and significance of the pre-metastatic niche. *Cancer Cell* **30**, 668–681 (2016).

28. Peinado, H. et al. Pre-metastatic niches: organ-specific homes for metastases. *Nat. Rev. Cancer* **17**, 302–317 (2017).

29. Pommier, A. et al. Unresolved endoplasmic reticulum stress engenders immune-resistant, latent pancreatic cancer metastases. *Science* **360**, eaao4908 (2018).

30. Lochner, M., Berod, L. & Sparwasser, T. Fatty acid metabolism in the regulation of T cell function. *Trends Immunol.* **36**, 81–91 (2015).

31. Ibrahim, J. et al. Dendritic cell populations with different concentrations of lipid regulate tolerance and immunity in mouse and human liver. *Gastroenterology* **143**, 1061–1072 (2012).

32. Henning, J. R. et al. Dendritic cells limit fibroinflammatory injury in nonalcoholic steatohepatitis in mice. *Hepatology* **58**, 589–602 (2013).

33. Sutti, S. & Albano, E. Adaptive immunity: an emerging player in the progression of NAFLD. *Nat. Rev. Gastroenterol. Hepatol.* **17**, 81–92 (2020).

34. Wang, G. et al. Tumour extracellular vesicles and particles induce liver metabolic dysfunction. *Nature* **618**, 374–382 (2023).

35. Di Biase, S. et al. Creatine uptake regulates CD8 T cell antitumor immunity. *J. Exp. Med.* **216**, 2869–2882 (2019).

36. Geroldinger, A., Lusa, L., Nold, M. & Heinze, G. Leave-one-out cross-validation, penalization, and differential bias of some prediction model performance measures-a simulation study. *Diagn. Progn. Res.* **7**, 9 (2023).

Linda Bojmar [1,2,31], Constantinos P. Zambirinis [2,3,4,31], Jonathan M. Hernandez[3,5,31], Jayasree Chakraborty[3,6], Lee Shaashua[1], Junbum Kim [7], Kofi Ennu Johnson[1], Samer Hanna[1], Gokce Askan[6,8], Jonas Burman [1,2], Hiranmayi Ravichandran[7,9], Jian Zheng[3], Joshua S. Jolissaint[1,3], Rami Srouji[1,3], Yi Song[3], Ankur Choubey [3], Han Sang Kim[1], Michele Cioffi[1], Elke van Beek[3], Carlie Sigel[6,8], Jose Jessurun [10], Paulina Velasco Riestra [2], Hakon Blomstrand [2,11], Carolin Jönsson[2], Anette Jönsson[2], Pernille Lauritzen[1], Weston Buehring[1], Yonathan Ararso[1], Dylanne Hernandez[1], Jessica P. Vinagolu-Baur[1], Madison Friedman[1], Caroline Glidden[1], Laetitia Firmenich[1], Grace Lieberman[1], Dianna L. Mejia[1], Naaz Nasar [3], Anders P. Mutvei[12], Doru M. Paul[13], Yaron Bram[14], Bruno Costa-Silva[1], Olca Basturk [6,8], Nancy Boudreau[1], Haiying Zhang[1], Irina R. Matei [1], Ayuko Hoshino[1], David Kelsen[6,15], Irit Sagi[16], Avigdor Scherz [17], Ruth Scherz-Shouval [18], Yosef Yarden [16], Moshe Oren [19], Mikala Egeblad[20], Jason S. Lewis [21,22], Kayvan Keshari[6,21], Paul M. Grandgenett[23], Michael A. Hollingsworth [23], Vinagolu K. Rajasekhar[24], John H. Healey [24], Bergthor Björnsson [2], Diane M. Simeone [25], David A. Tuveson[20], Christine A. Iacobuzio-Donahue [6,8,26], Jaqueline Bromberg [15,27], C. Theresa Vincent[12,28], Eileen M. O'Reilly [6,13,22], Ronald P. DeMatteo[3], Vinod P. Balachandran [3,6,29], Michael I. D'Angelica[3,6], T. Peter Kingham[3,6], Peter J. Allen[3], Amber L. Simpson [3], Olivier Elemento [7,9], Per Sandström[2], Robert E. Schwartz [14,30,32], William R. Jarnagin[3,6,32] & David Lyden [1,6,32]✉

[1]Departments of Pediatrics and Cell and Developmental Biology, Children's Cancer and Blood Foundation Laboratories, Drukier Institute for Children's Health, Meyer Cancer Center Weill Cornell Medicine, New York, NY, USA. [2]Department of Biomedical and Clinical Sciences, Linköping University, Linköping, Sweden. [3]Hepatopancreatobiliary Service, Department of Surgery, Memorial Sloan Kettering Cancer Center, New York, NY, USA. [4]Division of Surgical Oncology, Rutgers Cancer Institute of New Jersey, New Brunswick, NJ, USA. [5]Thoracic and Gastrointestinal Oncology Branch, National Cancer Institute, National Institutes of Health, Bethesda, MD, USA. [6]David M. Rubenstein Center for Pancreatic Cancer Research, Memorial Sloan Kettering Cancer Center, New York, NY, USA. [7]Department of Physiology and Biophysics, Institute for Computational Biomedicine, Weill Cornell Medicine, New York, NY, USA. [8]Department of Pathology, Memorial Sloan Kettering Cancer Center, New York, NY, USA. [9]Caryl and Israel Englander Institute for Precision Medicine, Weill Cornell Medicine, New York, NY, USA. [10]Department of Pathology and Laboratory Medicine, Weill Cornell Medicine, New York, NY, USA. [11]Department of Clinical Pathology, Linköping University, Linköping, Sweden. [12]Department of Laboratory Medicine, Division of Pathology, Karolinska Institutet, Stockholm, Sweden. [13]Division of Hematology and Medical Oncology, Department of Medicine, Weill Cornell Medicine, New York, NY, USA. [14]Division of Gastroenterology & Hepatology, Weill Cornell Medicine, New York, NY, USA. [15]Department of Medicine, Memorial Sloan Kettering Cancer Center, New York, NY, USA. [16]Department of Biological Regulation, Weizmann Institute of Science, Rehovot, Israel. [17]Department of Plant and Environmental Sciences, Weizmann Institute of Science, Rehovot, Israel. [18]Department of Biomolecular Sciences, Weizmann Institute of Science, Rehovot, Israel. [19]Department of Molecular Cell Biology, Weizmann Institute of Science, Rehovot, Israel. [20]Cold Spring Harbor Laboratory, Cold Spring Harbor, NY, USA. [21]Radiology and Molecular Pharmacology Program, Memorial Sloan Kettering Cancer Center, New York, NY, USA. [22]Weill Cornell Medical College, New York, NY, USA. [23]Eppley Institute for Research in Cancer and Allied Diseases, Fred & Pamela Buffett Cancer Center, University of Nebraska Medical Center, Omaha, NE, USA. [24]Orthopedic Service, Department of Surgery, Memorial Sloan Kettering Cancer Center, New York, NY, USA. [25]Perlmutter Cancer Center, New York University Langone Health, New York, NY, USA. [26]Human Oncology and Pathogenesis Program, Memorial Sloan Kettering Cancer Center, New York, NY, USA. [27]Department of Medicine, Weill Cornell Medicine, New York, NY, USA. [28]Department of Microbiology, New York University Grossman School of Medicine, New York, NY, USA. [29]Immuno-Oncology Service, Human Oncology and Pathogenesis Program, Memorial Sloan Kettering Cancer Center, New York, NY, USA. [30]Department of Biomedical Engineering, Cornell University, Ithaca, NY, USA. [31]These authors contributed equally: Linda Bojmar, Constantinos P. Zambirinis, Jonathan M. Hernandez. [32]These authors jointly supervised this work: Robert E. Schwartz, William R. Jarnagin, David Lyden. ✉e-mail: dcl2001@med.cornell.edu

Methods

Study design and patients

We performed a prospective observational study of 68 patients subjected to pancreatic resection at Memorial Sloan Kettering Cancer Center (MSKCC) between 2015 and 2018. Patients 18 years or older with presumed resectable pancreatic adenocarcinoma according to National Comprehensive Cancer Network guidelines (PaC group) or pancreatic/peri-pancreatic benign or pre-malignant lesions (non-PaC group) were eligible for the study. Patients who had received neoadjuvant therapy and those with unresectable or metastatic disease or a cancer diagnosis other than pancreatic ductal adenocarcinoma (for example, acinar cell carcinoma and intraductal papillary mucinous neoplasms (IPMNs) with associated colloid carcinoma) were excluded.

The collection and analysis of human blood, tumor and liver tissue was approved by the institutional review boards (IRBs) of MSKCC (IRB no. 15-015) and Weill Cornell Medicine (WCM) (IRB no. 0604008488) (ClinicalTrials.gov registration: NCT02393703). All patients presenting in the MSKCC hepatopancreatobiliary (HPB) clinic for possible pancreatectomy who met inclusion criteria were screened and considered for recruitment at the discretion of the operative surgeon. All individuals who agreed to participate provided informed consent. The study is compliant with all relevant ethical regulations regarding research involving human subjects. The sex of the included patients is reported in Supplementary Table 1 and is in line with the established slightly higher incidence of PaC in males. Sex assignment was based on a self-reported questionnaire asking for sex at birth, as documented in the patient medical records. Gender or race data were not collected because they were not readily available from the medical records. No attempt to select patients on a race, sex and/or gender basis was made.

Clinical outcomes and recurrence groups

All patients underwent routine peri-operative clinical care and radiologic follow-up according to our institutional standards[37]. Recurrence data were collected from medical records. The date and site of first metastatic recurrence were defined as the date a lesion was first detected on cross-sectional imaging, even if it was initially indeterminate and later classified as a recurrence on subsequent imaging and/or biopsy. Follow-up data were collected up to the occurrence of LiM or death; otherwise, patients were censored at 36 months. Time to first recurrence and TTLiM were calculated from the day of resection. Patients who developed LiM as first site of recurrence (with or without simultaneous EHM recurrence) were classified as LiM<6 or LiM>6, depending on whether LiM occurred within 6 months of resection or beyond 6 months, respectively. Patients with EHM-only recurrence at any time during follow-up were classified as EHM. Isolated local recurrences were classified separately. Patients without clinical or radiologic evidence of recurrence over follow-up were classified as NED.

Tissue collection and processing

Three geographically distinct incisional liver biopsies without any gross evidence of metastasis were obtained at the time of surgery and transferred on ice directly to the laboratory. Millimeter-sized pieces were frozen on liquid nitrogen for downstream RNA and metabolite extractions. When sufficient liver material was available, a fresh portion was immediately processed for flow cytometry and/or cryopreserved for scRNA-seq.

Histology, immunohistochemistry and immunofluorescence

For histologic analyses, liver biopsies were washed in PBS and fixed in 4% PFA/PBS overnight at 4 °C, followed by multiple washes in cold PBS before being transferred to cold 70% ethanol. Tissues were dehydrated and embedded in paraffin and sectioned into 4-μm sections.

Formalin-fixed, paraffin-embedded (FFPE) tissues were stained by conventional hematoxylin and eosin (H&E) protocols and Masson's trichrome. Two independent expert liver pathologists (G.A. and J.J.) examined the stained slides in a blinded fashion and graded fibrosis, steatosis and inflammation (portal and lobular) according to standardized scores for reporting hepatic pathology[11].

Next, 4-μm FFPE sections were stained for immunohistochemistry (IHC) and immunofluorescence (IF) manually or at the Molecular Core Facility of MSKCC using a Discovery XT processor or an Ultra processor (Ventana Medical Systems-Roche). Ki-67, IBA-1 and CD45 were stained by IHC according to the following protocol. After 32 min of heat and Cell Conditioning 1 (CC1, Ventana Medical Systems, 950-500) retrieval, the tissue sections were blocked first for 30 min in background blocking reagent (Innovex, NB306). A rabbit monoclonal anti-Ki-67 (clone SP6, Abcam, 16667) was used at 2.5 μg ml^{-1} concentration and incubated for 6-h incubation. A rabbit polyclonal anti-IBA-1 (Wako, 019-19741) was used in a concentration of 0.1 μg ml^{-1} for 5-h incubation. A mouse monoclonal anti-CD45 (clone 2B11, Dako, M0701) was used at 2.5 μg ml^{-1} concentration and incubated for 6-h incubation. Thereafter, primary antibodies were followed by 60 min of biotinylated goat anti-rabbit IgG (Vector Labs, PK6101) in 5.75 μg ml^{-1} concentration. Blocker D, Streptavidin-HRP D (part of the DAB Map Kit, Ventana Medical Systems) and the DAB Map Kit (760-124, Ventana Medical Systems) were prepared according to manufacturer instructions. The slides were counterstained with hematoxylin and coverslipped with Permount (Thermo Fisher Scientific). IHC for p53 was performed similarly using the undiluted ready-to-use clone DO-7 mouse monoclonal antibody (Dako, GA616), as described previously[38]. CD11B, CD68, CD206, CD3, CD8, NE, Ct-H3 and MPO were stained by IF. After 32 min of heat and CC1 (Ventana Medical Systems, 950-500) retrieval, the tissue sections were blocked first for 30 min in background blocking reagent (Innovex, NB306). The incubation with the primary antibodies was done for 6 h. A rabbit monoclonal CD11B antibody (clone EPR1344, Abcam, 133357) was used in 1 μg ml^{-1} concentration followed by 60-min incubation with biotinylated goat anti-rabbit IgG (Vector Labs, PK6101) in 5.75 μg ml^{-1}. Blocker D, Streptavidin-HRP and TSA A488 (Life Technologies, B40932) were prepared according to manufacturer instructions in 1:100 for 16 min. A mouse monoclonal anti-CD68 (clone KP1, Dako, M0814) was used in 0.02 μg ml^{-1}, followed by biotinylated anti-mouse secondary (Vector Labs, MOM Kit BMK-2202) in 5.75 μg ml^{-1}. Blocker D, Streptavidin-HRP and TSA CF594 (Biotium, 92174) were prepared according to manufacturer instructions in 1:2,000 for 16 min. A rabbit polyclonal anti-CD3 antibody (Dako, A0452) was used in 2.4 μg ml^{-1} concentration, followed by 60-min incubation with biotinylated goat anti-rabbit IgG (Vector Labs, PK6101) in 5.75 μg ml^{-1}. Streptavidin-HRP and TSA A488 (Life Technologies, B40932) were prepared according to manufacturer instructions in 1:100 for 16 min. A rabbit polyclonal anti-CD8 antibody (Cell Signaling Technology, 98941) was used in 4.8 μg ml^{-1} concentration, followed by 60-min incubation with biotinylated goat anti-rabbit IgG (Vector Labs, PK6101) in 5.75 μg ml^{-1}. Streptavidin-HRP and TSA CF594 (Biotium, 92174) were prepared according to manufacturer instructions in 1:2,000 for 16 min. All slides were counterstained in 5 μg ml^{-1} DAPI (Sigma-Aldrich, D9542) for 5 min at room temperature, mounted with anti-fade mounting medium Mowiol (Mowiol 4-88 (Calbiochem, 475904)) and coverslipped. For NET analysis, anti-NE / Neutrophil Elastase Sheep Anti-Human Polyclonal Antibody (LS-Bio, LS-B4244; dilution 1:200), anti-Ct-H3 / histone H3 (citrulline R2 + R8 + R17) rabbit antibody−ChIP grade (Abcam, ab5103; dilution 1:250) and anti-MPO / goat anti-myeloperoxidase (R&D Systems, AF3667; dilution 1:200) were used.

Quantifications of stains were performed by ImageJ and/or a blinded pathologist. Positive area, number of cells and localization were analyzed.

Tissue microarray construction and imaging mass cytometry

Two tissue microarrays (TMAs) were constructed from 37 patients (32 PaC−eight per recurrence group and five non-PaC) with sufficient

tissue to punch three cores of 1.5-mm diameter representing both portal and lobular areas, defined by a pathologist. TMAs were sectioned and confirmed by H&E staining and used for imaging mass cytometry. Then, 100 μg of purified antibody in BSA and azide-free format was conjugated using the Maxpar X8 Multimetal Labeling Kit (Fluidigm) as per the manufacturer's protocol (Supplementary Table 12). Sections were ablated on a Hyperion Imaging System (Fluidigm). Freshly cut 5-μm-thick FFPE sections were stored at 4 °C for 1 d before staining. Slides were first incubated for 1 h at 60 °C on a slide warmer, followed by dewaxing in fresh CitriSolv (Decon Labs) twice for 10 min and then rehydrated in descending series of 100%, 95%, 80% and 75% ethanol for 5 min each. After 5 min of Milli-Q water wash, the slides were treated with antigen retrieval solution (Tris-EDTA, pH 9.2) for 30 min at 96 °C. Slides were cooled to room temperature, washed twice in TBS and blocked for 1.5 h in Super-Block Solution (Thermo Fisher Scientific), followed by overnight incubation at 4 °C with the prepared antibody cocktail containing all metal-labeled antibodies in a humid chamber. The next day, slides were washed twice in 0.2% Triton X-100 in PBS and twice in TBS. DNA staining was performed using Intercalator-Iridium in PBS solution for 30 min in a humid chamber at room temperature. Slides were washed with Milli-Q water and air dried prior to ablation. The instrument was calibrated using a tuning slide to optimize the sensitivity of detection range. All ablations were performed with a laser frequency of 200 Hz. Tuning was performed intermittently to ensure that the signal detection integrity was within the detectable range. The raw MCD files were exported for further downstream processing.

Processing IMC data into AnnData single-cell matrix with spatial coordinates

We used the IMC package (https://github.com/ElementoLab/imc, version 0.1.4) to pre-process the raw MCD files into a combined AnnData object that contains the location and expression profiles of acquired cells. With original MCD files acquired through the Hyperion machine, regions of interest (ROIs) were extracted as stacks of images in .tiff file format along with associated metadata, including channel and epitope information. To reduce the images to three-dimensional conventional format, we used a pre-trained ilastik[39] model to predict a nuclear, cytoplasmic and background probability map. The probability map was subsequently segmented using DeepCell[40] to capture and identify cellular and nuclear borders.

To quantify cellular expressions, we used the cell masks to aggregate the mean intensity of pixels within a cell for each antibody channel through scikit-image. We combined the per-cell expression vector from all cells across all images into a single matrix through scanpy[41] in AnnData[42] format to process the data comprehensively and consistently. We then performed log transformation and z-score normalization with truncation at positive and negative 3 standard deviations, followed by Harmony[43] (version 0.3.0) batch correction to phase out sample-specific biases.

T cell phenotyping and spatial localization

To filter out the T cell population, we extracted cells that had CD3 expression that was more than 2 standard deviations after z-score normalization. This captured 36,987 cells (5.3%) out of 696,335 cells. For the extracted T cells, we performed principal component analysis, neighborhood calculation and Leiden clustering[44] to systematically and quantitatively identify the cell phenotypes captured in IMC with all markers combined across all images. These clusters were annotated into CD4, CD8, Treg and NKT/γδT cells based on their expression of CD3, CD4, CD8A, FoxP3, NKG2A and TRDC.

To identify the spatial localization of the T cells, we performed UTAG[45] with a max_dist of 20 and Leiden clustering at 0.1 and mapped the resulting three clusters to lobular or portal based on the whether the zones were KRT8/18 and ARG1 positive.

RNA-seq

mRNA-seq of liver biopsies was performed at Integrated Genomics Operation (IGO), MSKCC. In brief, total RNA from 5 mg of frozen liver tissue was extracted using an RNeasy Mini Kit (Qiagen, 74104) according to instructions provided by the manufacturer. After RiboGreen quantification and quality control (QC) analysis of 1 μg using a Total RNA Nano chip on an Agilent Bioanalyzer 2100, samples with RNA integrity number (RIN) values less than 3 were excluded. Samples underwent ribosomal depletion and library preparation using the TruSeq Stranded Total RNA LT Kit (Illumina, RS-122-1202) according to instructions provided by the manufacturer with 6–8 cycles of PCR. Samples were barcoded and run on a HiSeq 2500 in Rapid or High Output Mode or a HiSeq 4000 in a 50 bp/50 bp paired-end run, using the HiSeq Rapid SBS Kit v2, TruSeq SBS Kit v4 or HiSeq 3000/4000 SBS Kit, respectively (Illumina). On average, 88 million paired reads were generated per sample, and 32% of the data mapped to the transcriptome. Standard pipeline analyses were performed by IGO, and subsequent comparisons were performed by DESeq2, R software. log$_2$ fold changes exceeding 1/−1 with adjusted $P < 0.1$ (Wald test) were considered differentially expressed. Genes of interest were further confirmed by protein expressions and scRNA-seq. Heatmaps and hierarical clustering were generated by Morpheus (Broad Institute). GSEA using the Hallmarks of Cancer gene set (Molecular Signatures Database (MSigDB)) was performed to determine pathways differentially enriched between the groups ($P < 0.05$, false discovery rate (FDR) < 0.25). Gene clustering analysis and visualization were performed by Metascape version 3.5 and Cytoscape 3.5.1 ClueGO with the GO Immune System Process with a P value cutoff of <0.1.

Metabolomics

Metabolite extraction was performed on 24 PaC and nine non-PaC patients with enough liver biopsy material, as previously described[46]. In brief, 5 mg of liquid nitrogen snap-frozen liver tissue was submerged in 80% methanol and pestle-grinded on dry ice, followed by serial incubations and centrifugations to obtain a clear supernatant for lyophilization by SpeedVac. The samples were stored at −80 °C. Unlabeled polar metabolite profiling by liquid chromatography with tandem mass spectrometry (LC−MS/MS) was performed at Beth Israel Deaconess Medical Center, Harvard Medical School. In total, 296 metabolites were detected. Results are presented as peak area of total ion current. Data analyses were performed using MetaboAnalyst 4.0 and 5.0 (ref. 47).

Hepatic non-parenchymal cell isolation

Hepatic non-parenchymal cell (NPC) isolation for downstream single-cell studies was performed on a subset of patients with adequate liver tissue as follows. A portion of the specimen was minced with scissors to 1-mm pieces and digested in HBSS with 1 mg ml^{-1} Collagenase IV (Worthington) and 1 U ml^{-1} DNAse I (Roche) for 20 min at 37 °C with constant agitation. After washing and straining through a 70-μm mesh, the NPCs were separated by density gradient centrifugation with 40% OptiPrep solution as previously described[31]. Specifically, the cell suspension was combined with the OptiPrep, underlayed in GBSS buffer and spun at 900g for 20 min. The NPCs, which concentrated at the interface, were collected and subjected to red blood cell lysis using ACK lysis buffer (Gibco). Isolated NPCs were validated to be more than 90% CD45$^+$ cells by flow cytometry on a FACSCanto with FACSDiva software (BD Biosciences). Analysis was performed using FlowJo version 10 software.

scRNA-seq

The isolated hepatic NPCs (>90% CD45$^+$) were cryopreserved in 10% DMSO/90% FBS mix until the time of analysis. Upon retrieval, live cells were sorted by exclusion on ethidium homodimer-1 and gating on calcein violet, validated by trypan blue staining and submitted to downstream processing for scRNA-seq if viability was more than 80%.

Of the 10 tested patient samples, eight met the recommended cell concentration and viability criteria (6,000 cells per 50,000 reads) and were submitted for downstream analysis by 10x Genomics at the Epigenomics Core, WCM (Supplementary Table 3). Sequencing results were post-processed by Cell Ranger software (10x Genomics), subjected to ZINB-WaVE dimensional reduction[48] and further analyzed by the R Seurat pipeline (Satija laboratory). Unsupervised clustering of all cells combined after ZINB-WaVE dimensional reduction yielded six distinct clusters, with most cells expressing *PTPRC*/CD45, consistent with immune cell lineage (Extended Data Fig. 6a). The two major clusters consisted of myeloid cells (cluster 1; 4,747 cells) and lymphoid cells (cluster 5; 28,564 cells). Unsupervised subdivision of the main clusters at higher resolution (0.8) resulted in refinement of the lymphoid cluster into NK, NKT and T cell clusters and further division of the myeloid cluster into monocytes and myeloid DCs. Finally, supervised lineage marker-based clustering of the myeloid population yielded three subsets: CD14+ classical monocytes, CD16+ non-classical monocytes and CD1c+ myeloid DCs. The other initial clusters were defined as myeloid DC subset (CD1c−; cluster 2), lymphoid DCs (cluster 3), B cells (cluster 4) and a population of proliferating lymphoid cells (cluster 6). Subsequent analyses were done on CD3+ lymphoid clusters by subsetting after further integration and dimensional reduction visualized by uniform manifold approximation and projection (UMAP).

Deconvolution of RNA-seq data was performed by CIBERSORTx software with custom or the LM22 gene signature[23].

Statistical analysis

Statistical analysis was conducted using SPSS Statistics for Windows versions 25 and 26 (IBM) and GraphPad Prism version 9 for Windows (GraphPad Software). For nominal variables, Pearson's χ^2 test and Fisher's exact test were used. For ordinal variables, the Kruskal–Wallis test was used. Continuous variables that followed a normal distribution were compared using a pairwise *t*-test, whereas non-parametric tests (Mann–Whitney *U*-test or Kruskal–Wallis test) were used if the distribution was not normal. All tests were two-tailed, and results were considered statistically significant when $P \leq 0.05$. Data visualized in bar graphs represent biological replicates and are displayed as mean ± s.e.m., unless otherwise specified. Recurrence and survival analyses were conducted using Kaplan–Meier methods. HRs were calculated using the Cox proportional hazards model.

Development of prediction models

The modeling of potential predictive features of future metastasis was evaluated with multivariate analysis using a machine-learning-based classification technique. Four models (m1–m4) were designed to distinguish one recurrence group at a time: m1, LiM versus all; m2, early LiM (LiM<6) versus all; m3, EHM versus all; and m4, NED versus all. Feature selection for each model was performed using the minimum redundancy maximum relevance (MRMR) method[49]. A forward selection method was applied to determine the final feature set, in which features were sequentially added to an empty candidate set until the addition of further features did not decrease the misclassification error. The selected features were then included in designing the prediction model using a naive Bayes classifier.

To evaluate the performance of the selected features, the leave-one-out (LOO) method was applied considering the small sample size. The LOO is a form of cross-validation where one sample is used for testing and the remaining observations are used to train the model. This is repeated until all samples are explored as test data. The feature selection followed by model designing was performed with training data only and evaluated with test data.

Classification of patients into recurrence groups was performed by calculating a probability score with each of the four models. The result with the highest probability score was selected.

Reporting summary

Further information on research design is available in the Nature Portfolio Reporting Summary linked to this article.

Data availability

Gene expression data have been deposited to the National Institutes of Health Gene Expression Omnibus repository and can be accessed as GSE245535 (bulk mRNA-seq) and GSE267209 (scRNA-seq). Cytoscape ClueGO with GO Immune System Process was used for gene clustering (https://apps.cytoscape.org/apps/cluego), and Metascape (https://metascape.org/gp/index.html#/main/step1) was used for Gene Ontology analysis. Gene set enrichment analysis was performed using the Hallmark gene sets from the MSigDB (https://www.gsea-msigdb.org/gsea/msigdb/human/genesets.jsp?collection=H). The LM22 dataset was used for deconvolution of bulk mRNA-seq by CIBERSORTx (matrix provided in Supplementary_Tables_1.xlsx). Metabolomics source data can be accessed in Supplementary Dataset 1. Clinical data in this study can be found in Extended Data Table 1 and Supplementary Tables 1, 8 and 11.

Code availability

Code used for image quantifications and generation of the prediction models is available at https://github.com/czambir/PC_pml_code. Code used for imaging mass cytometry analysis can be found at https://github.com/ElementoLab/imc, version 0.1.4.

References

37. Allen, P. J. et al. Pasireotide for postoperative pancreatic fistula. *N. Engl. J. Med.* **370**, 2014–2022 (2014).
38. Attiyeh, M. A. et al. CT radiomics associations with genotype and stromal content in pancreatic ductal adenocarcinoma. *Abdom. Radiol. (NY)* **44**, 3148–3157 (2019).
39. Berg, S. et al. ilastik: interactive machine learning for (bio)image analysis. *Nat. Methods* **16**, 1226–1232 (2019).
40. Van Valen, D. A. et al. Deep learning automates the quantitative analysis of individual cells in live-cell imaging experiments. *PLoS Comput. Biol.* **12**, e1005177 (2016).
41. Wolf, F. A., Angerer, P. & Theis, F. J. SCANPY: large-scale single-cell gene expression data analysis. *Genome Biol.* **19**, 15 (2018).
42. Virshup, I., Rybakov, S., Theis, F. J., Angerer, P. & Wolf, F. A. anndata:Annotated data. Preprint at *bioRxiv* https://doi.org/10.1101/2021.12.16.473007 (2021).
43. Korsunsky, I. et al. Fast, sensitive and accurate integration of single-cell data with Harmony. *Nat. Methods* **16**, 1289–1296 (2019).
44. Traag, V. A., Waltman, L. & van Eck, N. J. From Louvain to Leiden: guaranteeing well-connected communities. *Sci. Rep.* **9**, 5233 (2019).
45. Kim, J. et al. Unsupervised discovery of tissue architecture in multiplexed imaging. *Nat. Methods* **19**, 1653–1661 (2022).
46. Yuan, M., Breitkopf, S. B., Yang, X. & Asara, J. M. A positive/negative ion-switching, targeted mass spectrometry-based metabolomics platform for bodily fluids, cells, and fresh and fixed tissue. *Nat. Protoc.* **7**, 872–881 (2012).
47. Chong, J. et al. MetaboAnalyst 4.0: towards more transparent and integrative metabolomics analysis. *Nucleic Acids Res.* **46**, W486–W494 (2018).
48. Risso, D., Perraudeau, F., Gribkova, S., Dudoit, S. & Vert, J. P. A general and flexible method for signal extraction from single-cell RNA-seq data. *Nat. Commun.* **9**, 284 (2018).
49. Peng, H., Long, F. & Ding, C. Feature selection based on mutual information: criteria of max-dependency, max-relevance, and min-redundancy. *IEEE Trans. Pattern Anal. Mach. Intell.* **27**, 1226–1238 (2005).

Acknowledgements

Author contributions

Competing interests

## Additional information

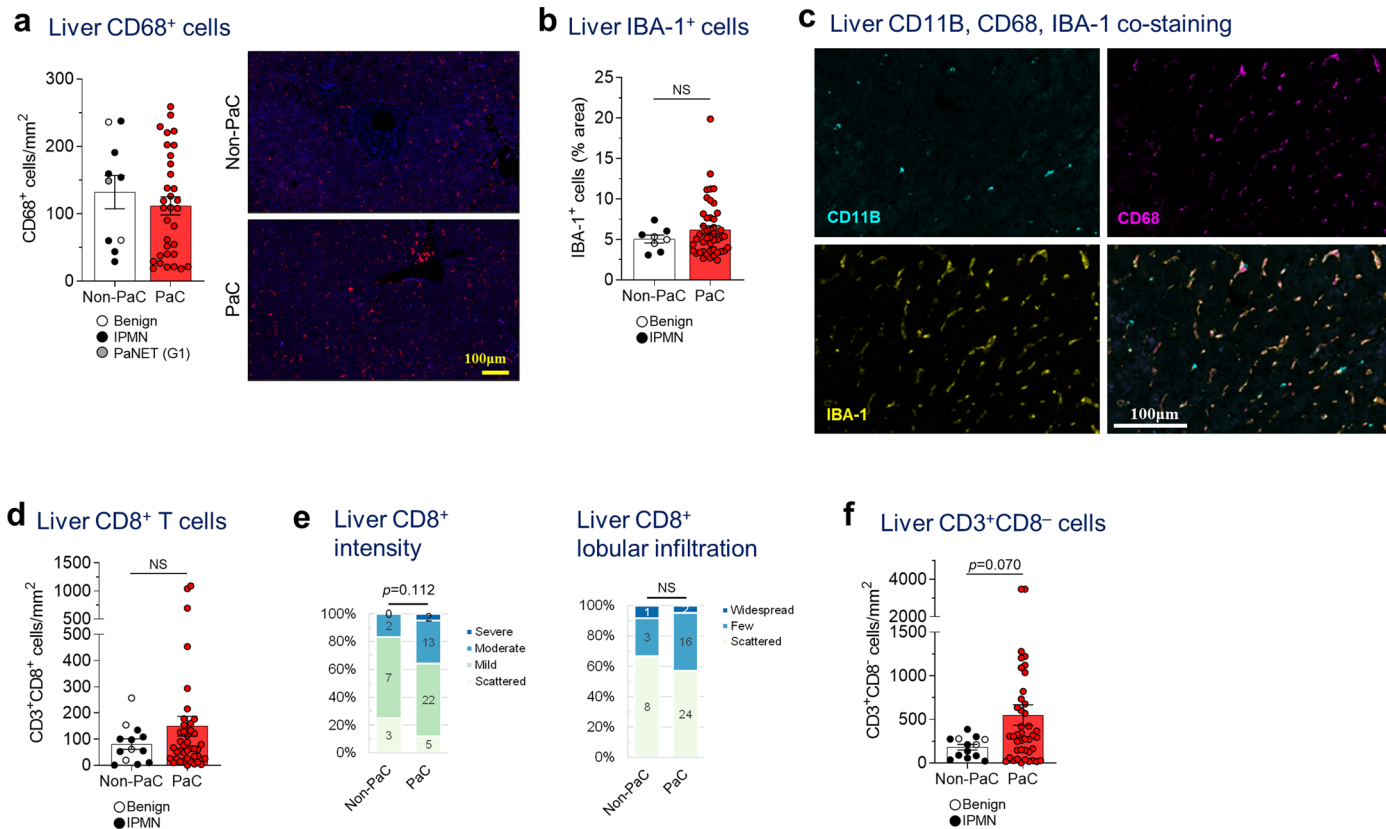**a** EHM *vs* NED

b Timing of LiM after resection
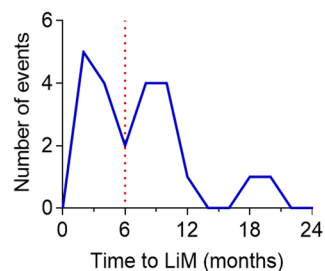
Extended Data Fig. 1 | Gene expression patterns in the liver associated with future recurrence. a, Immune cell gene clustering of the genes upregulated in EHM patients compared to NED (Cytoscape, ClueGO). **b**, Analysis of the timing of liver metastasis after resection of PaC demonstrated a pattern of an early peak of LiM, which occurred within 6 months of resection, followed by a second peak beyond 6 months.
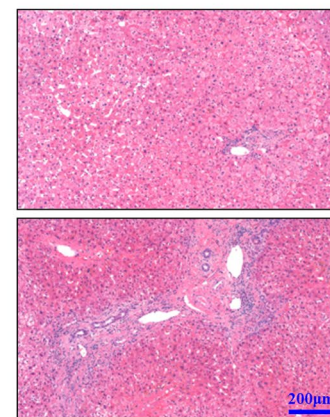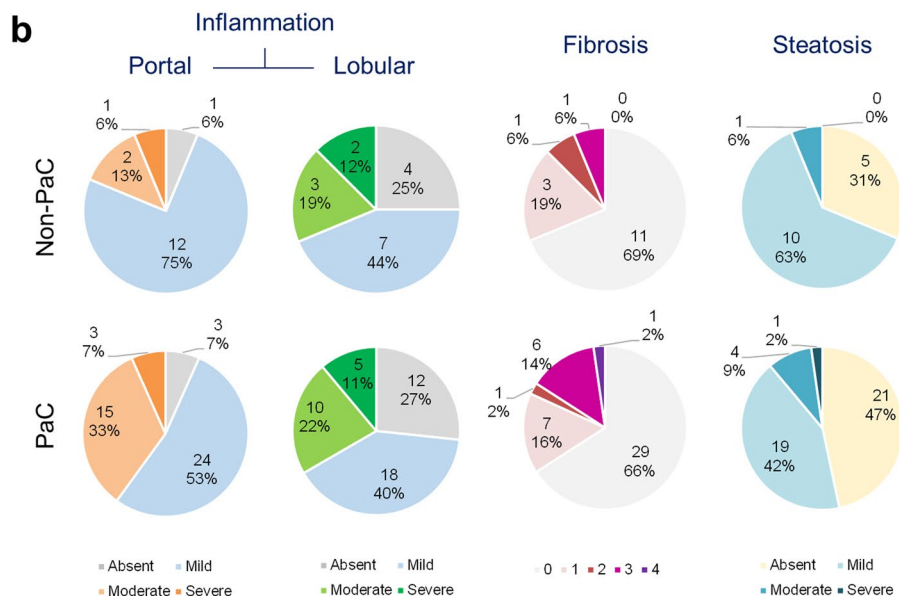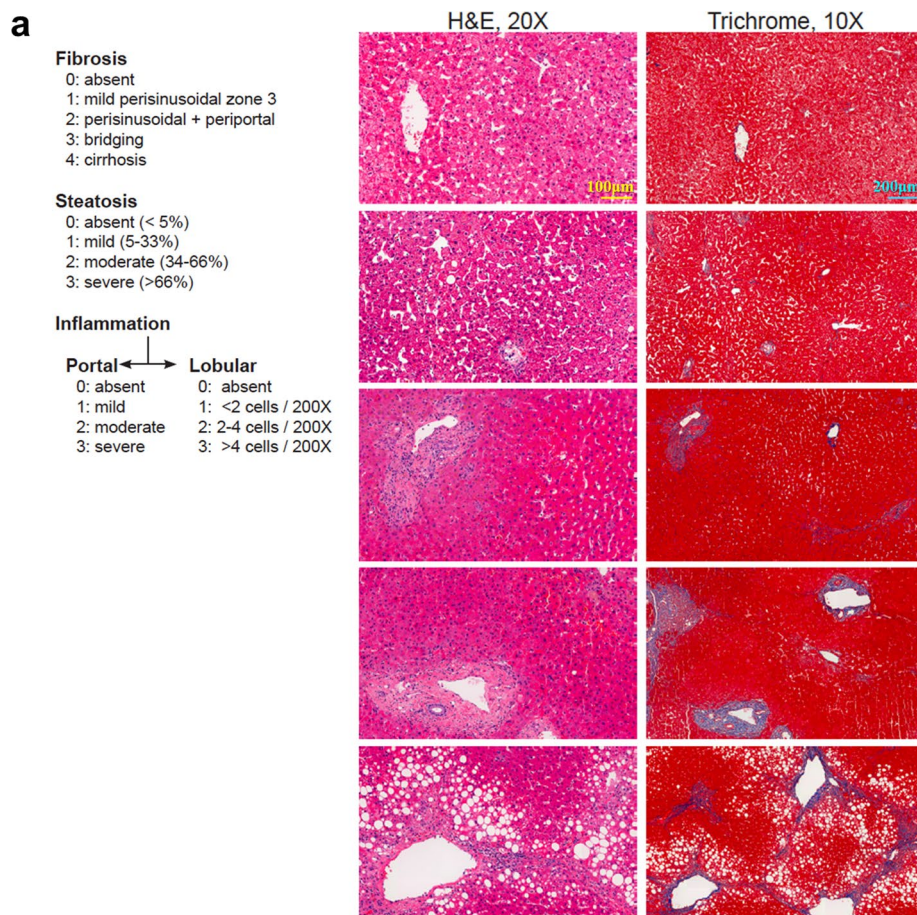
Extended Data Fig. 2 | Liver histology scoring. a-b, Liver fibrosis, steatosis, and inflammation were scored by two blinded pathologists and compared between PaC and Non-PaC. No statistically significant differences were noted (Somer's d test: portal inflammation, p = 0.361; lobular inflammation, p = 0.986; fibrosis, p = 0.695; steatosis, p = 0.442).

a Liver CD68+ cells

b Liver IBA-1+ cells

c Liver CD11B, CD68, IBA-1 co-staining

d Liver CD8+ T cells

**e** Liver CD8+ intensity — Liver CD8+ lobular infiltration

f Liver CD3+CD8− cells

Extended Data Fig. 3 | Liver immune cell characterization. a, Liver biopsies stained by immunofluorescence (IF) for CD68, quantified using ImageJ and compared between PaC (n = 33) and Non-PaC (n = 10; Mann-Whitney U-test; p = 0.356). **b**, Liver biopsies were stained by immunohistochemistry (IHC) for the macrophage activation marker IBA-1. The percentage of stained area was quantified with ImageJ and compared between PaC (n = 45) and Non-PaC (n = 8; Mann-Whitney U-test; p = 0.687). **c** Liver biopsies were co-stained by IF for CD11B, CD68, and IBA-1 to assess for overlap of these markers (n = 3). **d-f**, Liver biopsies were co-stained by IF for CD3 and CD8 as in Fig. 2e,f. **d**, CD3 + CD8 + T cells were quantified using ImageJ and compared between PaC (n = 42) and Non-PaC (n = 13; Mann-Whitney U-test; p = 0.565). **e**, The intensity of CD8 staining and the degree of CD8 + T cell lobular infiltration in PaC livers (n = 42) were assessed by a blinded pathologist and compared to non-PaC livers (n = 12; Somers' d; p = 0.112 and p = 0.648, respectively). **f**, CD3 + CD8− lymphocytes were quantified using ImageJ and compared between PaC (n = 42) and Non-PaC (n = 13; Mann-Whitney U-test; p = 0.070). Mean ± SEM are shown in bar graphs.
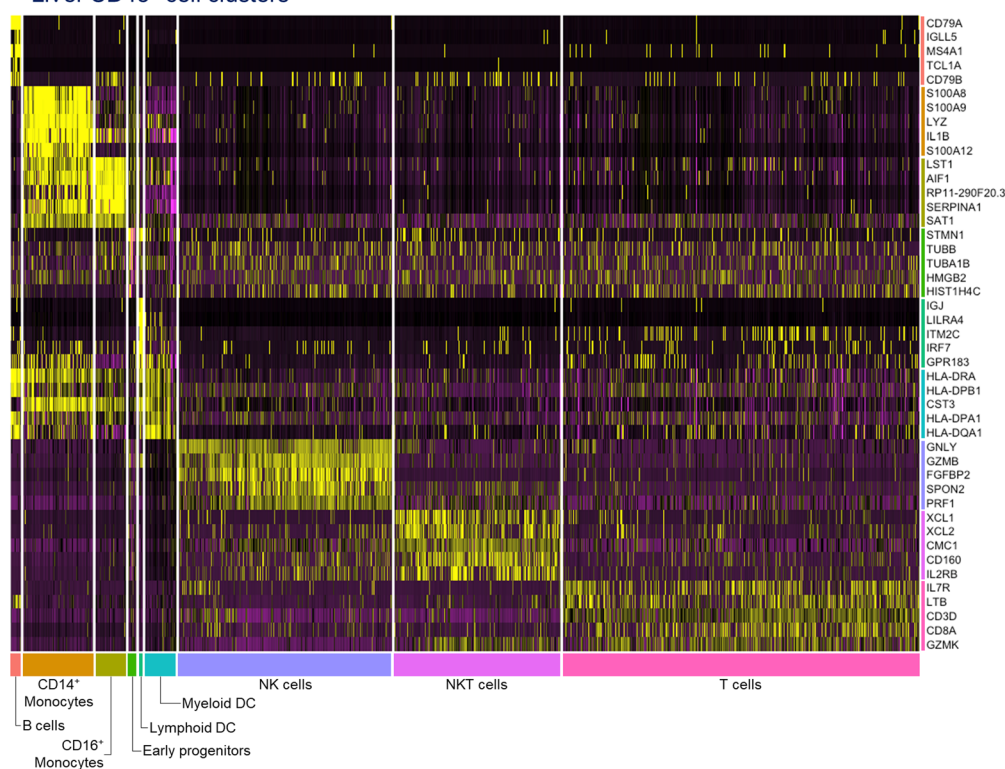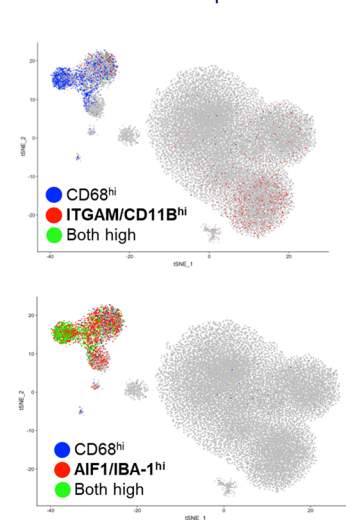
a Liver CD45+ cell clusters
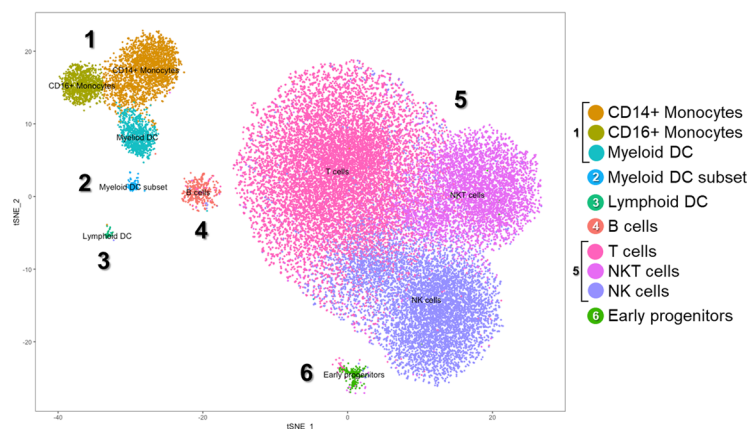
b Immune cell markers
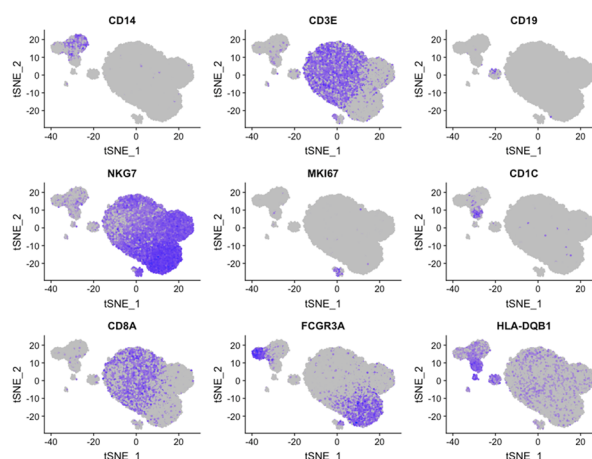

c Liver CD45+ cell clusters

**d** ITGAM/CD11B, CD68, and AIF1/IBA-1 co-expression

Extended Data Fig. 4 | Single cell RNA sequencing (scRNAseq) of liver immune cells. a, Hepatic NPCs (>95% CD45+) were isolated from 3 non-PaC and 5 PaC patients and subjected to scRNAseq. A total of 33,311 cells were sequenced, with 48,294 mean reads per cell and 1,000 median genes per cell detected. The sequencing saturation was >78% for all samples. a, tSNE plot combining all samples showing clustering into 10 major cell clusters. **b,** Distribution of gene expression of conventional immune cell markers further defining the different cell types. **c,** Heatmap of top 5 genes assigning the main cell types. **d,** Co-expression of CD11B/ITGAM, CD68, and IBA-1/AIF1 was assessed at the gene level, revealing CD11B expression predominantly by the CD14+ monocyte subset of the myeloid cluster and by the NK cell subset of the lymphoid cluster, showing little co-expression with CD68 (top tSNE plot). IBA-1 was expressed by all 3 subsets of the myeloid cluster, and most CD68-expressing cells (bottom tSNE plot).
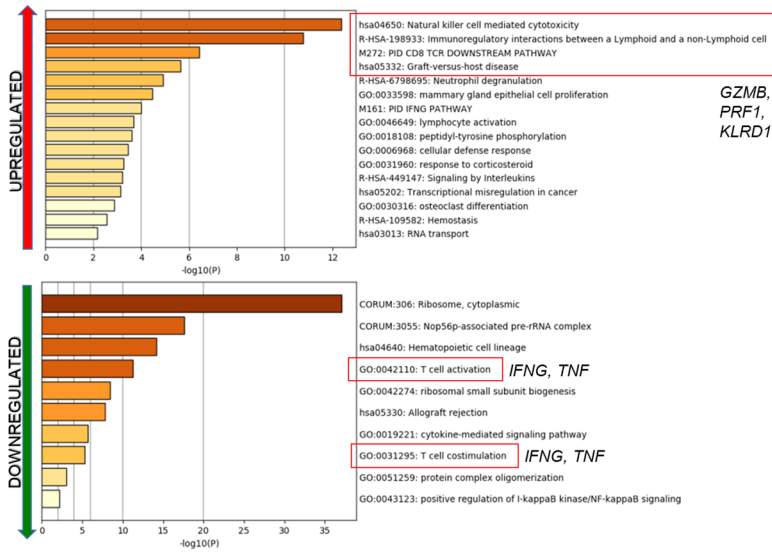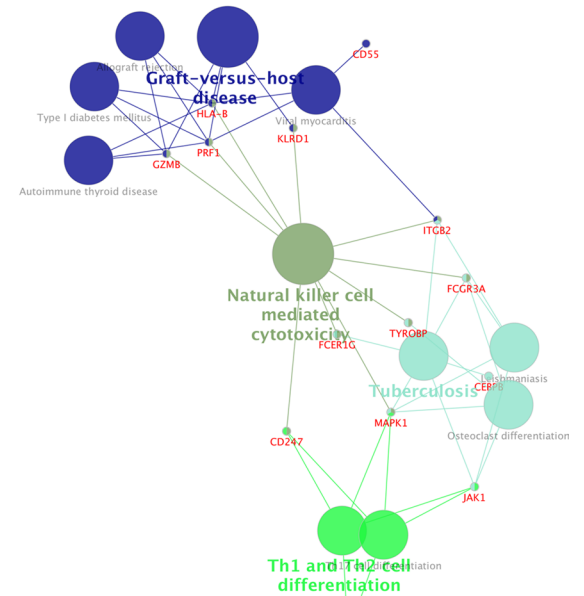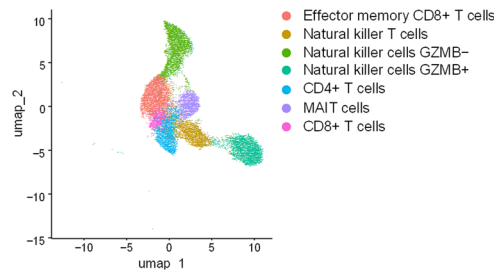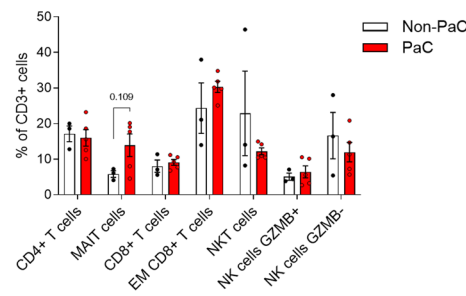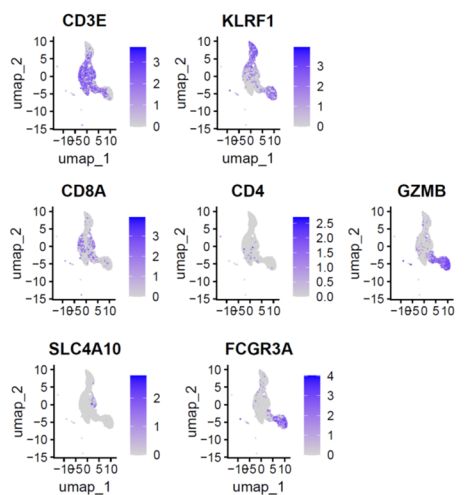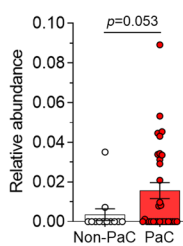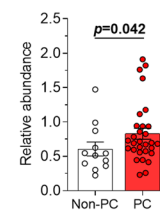
Extended Data Fig. 5 | scRNAseq of liver immune cells showing altered NK cell subsets. a, GO pathway analysis (Metascape) of the upregulated genes (upper panel) and downregulated genes (lower panel; cutoff p < 0.1, after adjustment for multiple comparisons). **b**, Immune cell gene clustering (Cytoscape, ClueGO) of genes upregulated in CD11B + NK cells in PaC vs non-PaC (cutoff p < 0.1, after adjustment for multiple comparisons). **c**–**e**, Sub-analysis of the lymphoid cluster (corresponding to cluster 5 of Extended Data Fig. 5a) to explore subsets of CD3-expressing lymphocytes demonstrated 7 sub-clusters (MAIT, mucosa-associated invariant T cells). c. Key defining genes are shown in d and in Fig. 3i. e, The relative proportion of these subclusters was compared between PaC and Non-PaC (multiple t-tests with correction for multiple comparisons, shown if p < 0.25). **f**, Cibersort-based deconvolution of the bulk liver mRNA sequencing data using the LM22 immune cell reference gene set for activated NK cells (PaC, n = 31; Non-PaC, n = 12; Mann-Whitney U-test, p = 0.053, Cibersort). **g** Cibersort-based deconvolution of the bulk liver mRNA sequencing data using the T/NKT immune cell gene set derived in Extended Data Fig. 4 (PaC, n = 30; Non-PaC, n = 12; Mann-Whitney U-test, p = 0.042). Mean ± SEM are shown in bar graphs.

a IMC: Liver CD3+ cell subset characterization
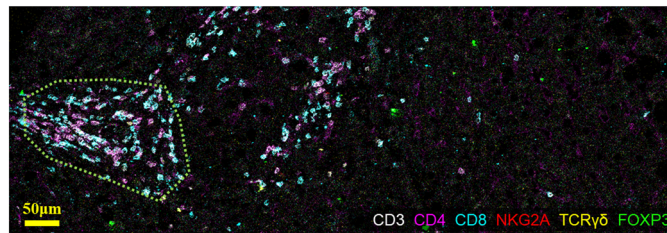
b IMC: Liver CD3+ cell subsets
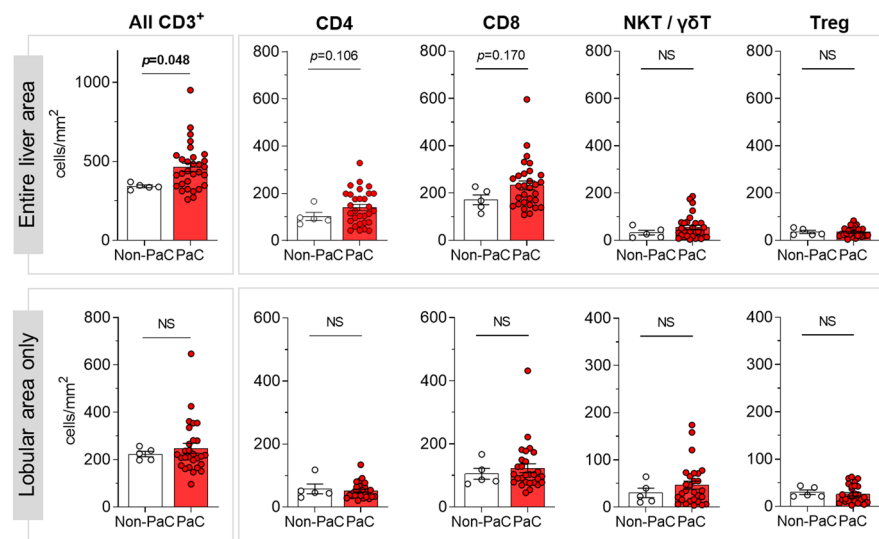
Extended Data Fig. 6 | Imaging mass cytometry for characterization of CD3+ cell subsets. Imaging mass cytometry (IMC) was performed on a tissue microarray including 2-3 cores per patient from 5 Non-PaC and 30 PaC patients. **a**, Representative image from a patient with LiM>6 demonstrating the staining pattern and the spatial distribution. For calculation of lobular cell densities, portal areas (enclosed in dotted line here) were segmented and subtracted from the total cell count for each patient. **b**, Subsets of CD3+ cells in the entire liver section, or in the lobular areas only, were compared between PaC and non-PaC: CD3+, p = 0.048 (total) and p = 0.981 (lobular; Mann-Whitney U-test); CD4+, p = 0.048 (total) and p = 0.742 (lobular; t-test); CD8+, p = 0.170 (total) and p = 0.715 (lobular; Mann-Whitney U-test); NKT/γδT (TCRγδ+ and/or NKG2A+), p = 0.477 (total) and p = 0.604 (lobular; Mann-Whitney U-test); Treg (FOXP3+), p = 0.727 (total) and p = 0.448 (lobular; Mann-Whitney U-test). Mean ± SEM are shown in bar graphs. Only p < 0.25 are shown on the graphs.
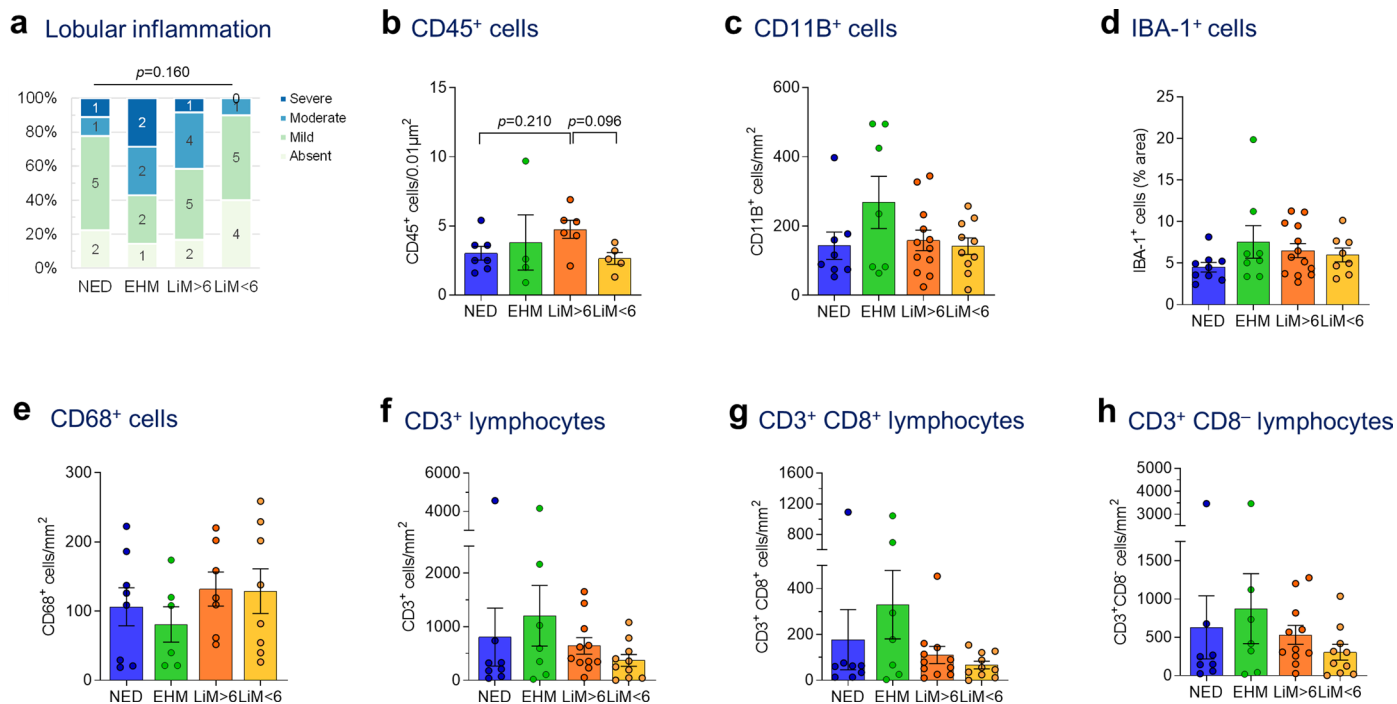
Extended Data Fig. 7 | Liver immune cells among recurrence groups.
a, Liver biopsies obtained at the time of resection from patients with NED, or distant recurrence (EHM, LiM>6, or LiM<6) were manually scored by a blinded pathologist for lobular inflammation (Kruskal-Wallis test). **b-h**, Liver biopsies were stained by IHC (b, d) or IF (c, e-h) for different immune cell markers, quantified using ImageJ and compared between the defined PaC recurrence pattern groups (ANOVA and pair-wise t-tests with multiple comparison correction by FDR; only p-values < 0.25 are shown). Mean ± SEM are shown in bar graphs. b, CD45$^+$ cells (n = 22; ANOVA p = 0.161). c, CD11B$^+$ cells (n = 37; ANOVA p = 0.504). d, IBA1$^+$ cells (n = 38; ANOVA p = 0.185). e, CD68$^+$ cells (n = 29; ANOVA p = 0.544). f, CD3$^+$ cells (n = 36; ANOVA p = 0.335). g, CD3$^+$CD8$^+$ cells (n = 36; ANOVA p = 0.289). h, CD3$^+$CD8$^-$ cells (n = 36; ANOVA p = 0.420).

a Liver Steatosis and Recurrence Patterns
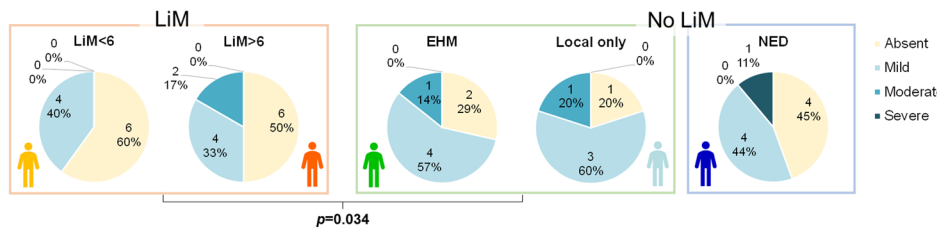
b Liver Steatosis: time-to-LiM
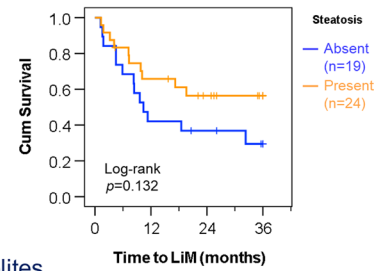
c Creatine-correlated metabolites
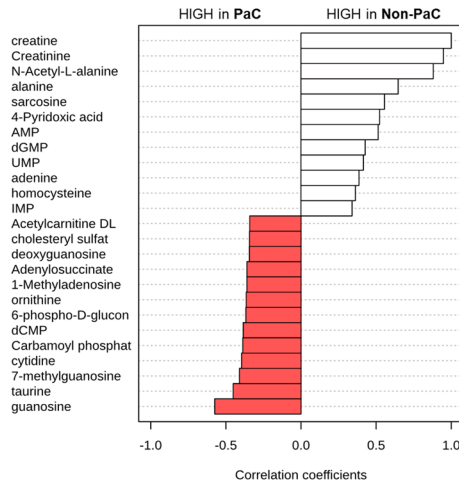
d Arginine and Proline pathway metabolites

e PaC vs Non-PaC: Serum Creatinine
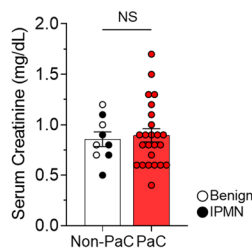
f Liver metabolomics and recurrence patterns
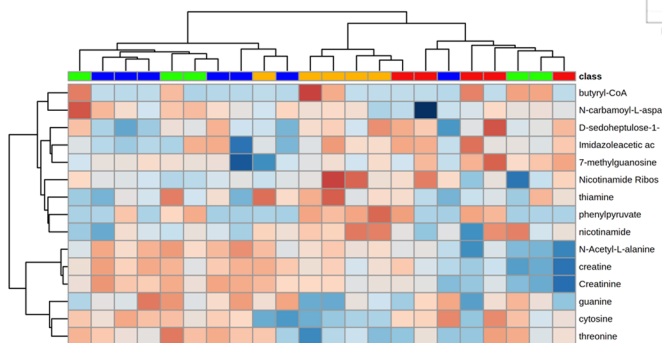
g Liver creatine and recurrence patterns
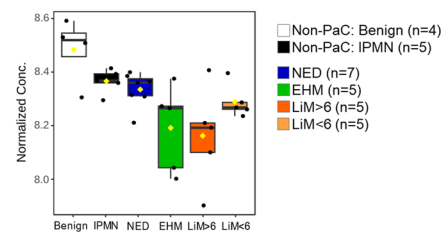
Extended Data Fig. 8 | Metabolic dysregulations in the pre-metastatic liver. **a**, Liver steatosis, graded at the time of resection, was examined separately among patients with LiM (LiM<6 and LiM>6), and patients without LiM (either distant EHM or isolated local recurrence) or disease-free during follow-up (NED). Patients who developed LiM had significantly less steatosis compared to those who developed recurrence at other sites (either distant EHM or isolated local recurrence) which correlated with the severity of metastatic pattern (LiM<6 being the worst and isolated local recurrence being the best prognostic group, based on overall survival outcomes [not shown]; Somer's d test; p = 0.034). **b**, Kaplan-Meier curve of time to LiM in patients with (n = 24) or without (n = 19)

evidence of liver steatosis (Log-rank test). **c**, Top 25 metabolites correlated with creatine in the pre-metastatic liver and **d**, expression of metabolites in the arginine/proline pathway (PaC, n = 24; Non-PaC, n = 9; t-test with correction for multiple comparisons). **e**, Comparison of serum creatinine levels among patients who underwent liver metabolomic analysis showed no difference (PaC, n = 24; Non-PaC, n = 9; Mean ± SEM; t-test, p = 0.680). **f**, Top 15 metabolites separating the defined recurrence groups (EHM, n = 5; LiM<6, n = 5; LiM>6, n = 5; NED, n = 7), including creatine and **g**, comparison of creatine levels in all analyzed samples (ANOVA; p < 0.001, FDR = 0.229). Box plots represent Median±IQR, with whiskers at 95th percentiles.

Extended Data Table 1 | Clinicopathological characteristics of patients with PaC with different recurrence patterns (*n*=41)

	NED		EH only#		LM>6mo		LM<6mo		*p* value
Patients in group (% all)	9	24%	9	11%	13	20%	10	22%	
Male	6	67%	5	56%	10	77%	6	60%	0.732 ^1
Age - Median (Range)	65.1	(49-83.4)	71.6	(58.6-87.0)	67.5	(57.8-81.1)	67.7	(51.7-77.1)	0.545 ^2
BMI - Median (Range)	27.9	(24.1-35.0)	32.1	(22.3-37.2)	25.7	(19.5-39.0)	25.5	(20.0-32.4)	0.317 ^2
Biliary obstruction*	4	44%	5	56%	7	54%	8	80%	0.426 ^1
Preop. biliary drainage	4	44%	4	44%	4	31%	4	40%	0.897 ^1
Preop CA19-9 - Median (Range)	90	(<1-130)	147	(3-463)	211.5	(64-1406)	195	(35-1132)	0.368 ^4
Differentiation									**0.020 ^4**
Well	2	22%	0	0%	0	0%	0	0%	
Moderate	5	56%	7	78%	8	67%	4	40%	
Poor	2	22%	2	22%	4	33%	6	60%	
T-stage (per AJCC 8th ed.)									0.652 ^4
1 (≤2cm)	1	11%	1	11%	0	0%	0	0%	
2 (>2 and ≤4cm)	6	67%	5	56%	9	69%	8	80%	
3 (>4cm)	2	22%	2	22%	4	31%	2	20%	
4 (invasion of great vessels)	0	0%	1	11%	0	0%	0	0%	
N-stage (per AJCC 8th ed.)	6	67%	8	89%	8	61%	6	60%	0.286 ^4
0 (-ve LNs)	3	33%	1	11%	5	39%	4	40%	
1 (1-3 +ve LNs)	3	33%	2	22%	4	31%	4	40%	
2 (>3 +ve LNs)	3	33%	6	67%	4	31%	2	20%	
Lymphovascular invasion	7	78%	3	67%	10	77%	8	80%	0.912 ^1
Perineural invasion	9	100%	8	89%	13	100%	10	100%	0.303 ^1

Patients with isolated local recurrence (n=5) as well as patients with inadequate follow-up (n=3) are not shown.

* Biliary obstruction was defined by the presence of either (a) clinical/biochemical (based on abnormal total bilirubin) evidence of jaundice, or (b) preoperative biliary drainage procedure for the relief of biliary obstruction.

^Statistical tests: [1]Pearson's χ^2; [2]ANOVA; [3] Kruskal-Wallis; [4] Linear-by-Linear Association

nature portfolio

Corresponding author(s): David Lyden, William Jarnagin, Robert Schwartz

Last updated by author(s): May 9, 2024

Reporting Summary

Nature Portfolio wishes to improve the reproducibility of the work that we publish. This form provides structure for consistency and transparency in reporting. For further information on Nature Portfolio policies, see our Editorial Policies and the Editorial Policy Checklist.

Statistics

For all statistical analyses, confirm that the following items are present in the figure legend, table legend, main text, or Methods section.

n/a	Confirmed	
☐	☒	The exact sample size (*n*) for each experimental group/condition, given as a discrete number and unit of measurement
☒	☐	A statement on whether measurements were taken from distinct samples or whether the same sample was measured repeatedly
☐	☒	The statistical test(s) used AND whether they are one- or two-sided *Only common tests should be described solely by name; describe more complex techniques in the Methods section.*
☐	☒	A description of all covariates tested
☐	☒	A description of any assumptions or corrections, such as tests of normality and adjustment for multiple comparisons
☐	☒	A full description of the statistical parameters including central tendency (e.g. means) or other basic estimates (e.g. regression coefficient) AND variation (e.g. standard deviation) or associated estimates of uncertainty (e.g. confidence intervals)
☐	☒	For null hypothesis testing, the test statistic (e.g. *F*, *t*, *r*) with confidence intervals, effect sizes, degrees of freedom and *P* value noted *Give P values as exact values whenever suitable.*
☒	☐	For Bayesian analysis, information on the choice of priors and Markov chain Monte Carlo settings
☐	☒	For hierarchical and complex designs, identification of the appropriate level for tests and full reporting of outcomes
☐	☒	Estimates of effect sizes (e.g. Cohen's *d*, Pearson's *r*), indicating how they were calculated

Our web collection on statistics for biologists contains articles on many of the points above.

Software and code

Policy information about availability of computer code

Data collection	No software was used for data collection
Data analysis	R 3.6.3, R studio 1.1.463, MetaboAnalyst v.4.0 & 5.0, Morpheus, Cibersortx, Cytoscape 3.5.1, Metascape v.3.5, GSEA, Image J2 Fiji, SPSS v25&26, GraphPad Prism 9, Matlab R2017a, Harmony version 0.3.0. Custom code: https://github.com/ElementoLab/imc, version 0.1.4 and https://github.com/czambir/PC_pml_code

For manuscripts utilizing custom algorithms or software that are central to the research but not yet described in published literature, software must be made available to editors and reviewers. We strongly encourage code deposition in a community repository (e.g. GitHub). See the Nature Portfolio guidelines for submitting code & software for further information.

Data

Policy information about availability of data

All manuscripts must include a data availability statement. This statement should provide the following information, where applicable:
- Accession codes, unique identifiers, or web links for publicly available datasets
- A description of any restrictions on data availability
- For clinical datasets or third party data, please ensure that the statement adheres to our policy

Gene expression data has been deposited to the NIH GEO repository and can be accessed as GSE245535 (Bulk mRNAseq) and GSE267209 (single cell RNAseq). Cytoscape ClueGO with GO Immune system Process was used for gene clustering (https://apps.cytoscape.org/apps/cluego) and Metascape (https://metascape.org/

gp/index.html#/main/step1) was used for gene ontology analysis. Gene set enrichment analysis was performed using the Hallmark gene sets from MSigDB (https://www.gsea-msigdb.org/gsea/msigdb/human/genesets.jsp?collection=H). The LM22 dataset was used for deconvolution of bulk mRNAseq by Cibersortx (matrix provided in Supplementary_Tables_1.xlsx). Metabolomics source data can be accessed in Supplementary_Tables_1.xlsx. Clinical data in this study can be found in Extended Data Table 1, Supplementary Table S1, Supplementary Table S8 and Supplementary Table S11.

Research involving human participants, their data, or biological material

Policy information about studies with [human participants or human data](). See also policy information about [sex, gender (identity/presentation), and sexual orientation]() and [race, ethnicity and racism]().

Reporting on sex and gender	The sex of the included patients is reported in Supplementary Table S1 and is in line with the established slightly higher incidence of PaC in males. Sex assignment was based on self-reported questionnaire asking for sex at birth, as documented in the patient medical records. No attempt to select patients on a race, sex and/or gender basis was made.
Reporting on race, ethnicity, or other socially relevant groupings	Gender or race data have not been collected since they were not readily available from the medical records. No attempt to select patients on a race, sex and/or gender basis was made.
Population characteristics	Data regarding sex, age, and co-variates such as BMI, biliary obstruction, tumor stage, histologic subtype, differentiation, lymphovascular/perinural invasion are reported in Supplementary Table 1.
Recruitment	Patients with presumed diagnosis of resectable pancreatic cancer or non-cancerous pancreatic/peripancreatic diseases who were eligible for pancreatectomy at MSKCC and had no contraindication to liver biopsy were approached and recruited to the study after informed consent, under IRB protocol #15-015. All patients presenting in the MSKCC HPB clinic for possible pancreatectomy who met inclusion criteria were screened and considered for recruitment at the discretion of the operative surgeon. All individuals who agreed to participate provided informed consent. The study is compliant with all relevant ethical regulations regarding research involving human subjects. Details are found in the manuscript's Methods section.
Ethics oversight	The collection and analysis of human blood, tumor and liver tissue was approved by the Institutional Review Boards of MSKCC (IRB # 15-015) and Weill Cornell Medicine (IRB # 0604008488). All individuals provided informed consent. The study is compliant with all relevant ethical regulations regarding research involving human subjects.

Note that full information on the approval of the study protocol must also be provided in the manuscript.

Field-specific reporting

Please select the one below that is the best fit for your research. If you are not sure, read the appropriate sections before making your selection.

☒ Life sciences ☐ Behavioural & social sciences ☐ Ecological, evolutionary & environmental sciences

For a reference copy of the document with all sections, see [nature.com/documents/nr-reporting-summary-flat.pdf]()

Life sciences study design

All studies must disclose on these points even when the disclosure is negative.

Sample size	Given that this was a first-in-human study, with complex exploratory outcomes, no precise power calculations were performed. The sample size was approximated by attempting to have 10 patients per group and considering that some patients may not have adequate follow-up or sufficient material for certain experiments. Given the diverse nature of our findings, we are now running a prospective study in a much larger number of patients.
Data exclusions	Patients with diagnoses other than pancreatic ductal adenocarcinoma (mainly patients with colloid carcinoma) were excluded and replaced, as originally planned. Pancreatic cancer (PaC) patients who had inadequate follow-up were only included in the PaC vs Non-PaC comparisons and were excluded from analyses comparing different recurrence groups (as outlined in Figure 1).
Replication	Three liver biopsies were collected to ensure intra-patient reproducibility between samples. Several measures were confirmed by multiple methods (whole tissue RNA sequencing, scRNA sequencing, immunohistochemistry, imaging mass cytometry). Analysis was confirmed by automated quantifications and manual scoring for measures such as IHC.
Randomization	No randomization was needed since there was no intervention. Further, the analyses were performed prior to the occurrence of the final endpoint (timing and site of metastasis).
Blinding	See above. Lead investigators were blinded to outcome at time of data collection. The remaining involved personnel were entirely blinded to the samples they were processing or analyzing even after the outcomes were known. Manual pathological scorings were performed by blinded pathologists.

Behavioural & social sciences study design

All studies must disclose on these points even when the disclosure is negative.

Study description	*Briefly describe the study type including whether data are quantitative, qualitative, or mixed-methods (e.g. qualitative cross-sectional, quantitative experimental, mixed-methods case study).*
Research sample	*State the research sample (e.g. Harvard university undergraduates, villagers in rural India) and provide relevant demographic information (e.g. age, sex) and indicate whether the sample is representative. Provide a rationale for the study sample chosen. For studies involving existing datasets, please describe the dataset and source.*
Sampling strategy	*Describe the sampling procedure (e.g. random, snowball, stratified, convenience). Describe the statistical methods that were used to predetermine sample size OR if no sample-size calculation was performed, describe how sample sizes were chosen and provide a rationale for why these sample sizes are sufficient. For qualitative data, please indicate whether data saturation was considered, and what criteria were used to decide that no further sampling was needed.*
Data collection	*Provide details about the data collection procedure, including the instruments or devices used to record the data (e.g. pen and paper, computer, eye tracker, video or audio equipment) whether anyone was present besides the participant(s) and the researcher, and whether the researcher was blind to experimental condition and/or the study hypothesis during data collection.*
Timing	*Indicate the start and stop dates of data collection. If there is a gap between collection periods, state the dates for each sample cohort.*
Data exclusions	*If no data were excluded from the analyses, state so OR if data were excluded, provide the exact number of exclusions and the rationale behind them, indicating whether exclusion criteria were pre-established.*
Non-participation	*State how many participants dropped out/declined participation and the reason(s) given OR provide response rate OR state that no participants dropped out/declined participation.*
Randomization	*If participants were not allocated into experimental groups, state so OR describe how participants were allocated to groups, and if allocation was not random, describe how covariates were controlled.*

Ecological, evolutionary & environmental sciences study design

All studies must disclose on these points even when the disclosure is negative.

Study description	*Briefly describe the study. For quantitative data include treatment factors and interactions, design structure (e.g. factorial, nested, hierarchical), nature and number of experimental units and replicates.*
Research sample	*Describe the research sample (e.g. a group of tagged Passer domesticus, all Stenocereus thurberi within Organ Pipe Cactus National Monument), and provide a rationale for the sample choice. When relevant, describe the organism taxa, source, sex, age range and any manipulations. State what population the sample is meant to represent when applicable. For studies involving existing datasets, describe the data and its source.*
Sampling strategy	*Note the sampling procedure. Describe the statistical methods that were used to predetermine sample size OR if no sample-size calculation was performed, describe how sample sizes were chosen and provide a rationale for why these sample sizes are sufficient.*
Data collection	*Describe the data collection procedure, including who recorded the data and how.*
Timing and spatial scale	*Indicate the start and stop dates of data collection, noting the frequency and periodicity of sampling and providing a rationale for these choices. If there is a gap between collection periods, state the dates for each sample cohort. Specify the spatial scale from which the data are taken*
Data exclusions	*If no data were excluded from the analyses, state so OR if data were excluded, describe the exclusions and the rationale behind them, indicating whether exclusion criteria were pre-established.*
Reproducibility	*Describe the measures taken to verify the reproducibility of experimental findings. For each experiment, note whether any attempts to repeat the experiment failed OR state that all attempts to repeat the experiment were successful.*
Randomization	*Describe how samples/organisms/participants were allocated into groups. If allocation was not random, describe how covariates were controlled. If this is not relevant to your study, explain why.*
Blinding	*Describe the extent of blinding used during data acquisition and analysis. If blinding was not possible, describe why OR explain why blinding was not relevant to your study.*

Did the study involve field work? ☐ Yes ☐ No

Field work, collection and transport

Field conditions	*Describe the study conditions for field work, providing relevant parameters (e.g. temperature, rainfall).*
Location	*State the location of the sampling or experiment, providing relevant parameters (e.g. latitude and longitude, elevation, water depth).*
Access & import/export	*Describe the efforts you have made to access habitats and to collect and import/export your samples in a responsible manner and in compliance with local, national and international laws, noting any permits that were obtained (give the name of the issuing authority, the date of issue, and any identifying information).*
Disturbance	*Describe any disturbance caused by the study and how it was minimized.*

Reporting for specific materials, systems and methods

We require information from authors about some types of materials, experimental systems and methods used in many studies. Here, indicate whether each material, system or method listed is relevant to your study. If you are not sure if a list item applies to your research, read the appropriate section before selecting a response.

Materials & experimental systems

n/a	Involved in the study
☐	☒ Antibodies
☒	☐ Eukaryotic cell lines
☒	☐ Palaeontology and archaeology
☒	☐ Animals and other organisms
☐	☒ Clinical data
☒	☐ Dual use research of concern
☒	☐ Plants

Methods

n/a	Involved in the study
☒	☐ ChIP-seq
☒	☐ Flow cytometry
☒	☐ MRI-based neuroimaging

Antibodies

Antibodies used	A rabbit monoclonal anti-Ki-67 (clone SP6, abcam cat#16667) was used at 2.5μg/mL concentration and incubated for 6 hours incubation. A rabbit polyclonal anti-IBA-1 (Wako, cat#019-19741) was used in a concentration of 0.1μg/mL for 5 hours incubation. A mouse monoclonal anti-CD45 (clone 2B11, Dako cat#M0701) was used at 2.5μg/mL concentration and incubated for 6 hours incubation. Thereafter, both primary antibodies were followed by 60 minutes of biotinylated goat anti-rabbit IgG (Vector labs, cat.# PK6101) in 5.75 μg /ml concentration. Immunohistochemistry for p53 was performed similarly using the DO-7 mouse monoclonal antibody (Dako, cat# GA616), as described previously for FLEX ready-to-use antibodies (undiluted). CD11B, CD68, CD3, CD8, NE, ctH3 and MPO were stained by IF. The incubations with the primary antibodies were done for 6 hours. A rabbit monoclonal CD11B antibody (clone EPR1344, abcam cat#133357) was used in 1 μg/ml concentration followed by 60 minutes incubation with biotinylated goat anti-rabbit IgG (Vector labs, cat#PK6101) in 5.75μg /ml. A mouse monoclonal CD68 (clone KP1, Dako, cat#M0814) was used in 0.02μg /ml followed by biotinylated anti- mouse secondary (Vector Labs, MOM Kit BMK-2202) in 5.75 μg /ml. A rabbit polyclonal anti-CD3 antibody (Dako, cat#A0452) was used in 2.4 μg /ml concentrations followed by 60 minutes incubation with biotinylated goat anti-rabbit IgG (Vector labs, cat#PK6101) in 5.75 μg /ml. A rabbit polyclonal anti-CD8 antibody (Cell Signaling, cat#98941) was used in 4.8 μg /ml concentrations followed by 60 minutes incubation with biotinylated goat anti-rabbit IgG (Vector labs, cat#PK6101) in 5.75μg /ml. For NET analysis, NE (LS-Bio, LS-B4244), HNE / Neutrophil Elastase Sheep anti-Human Polyclonal Antibody (dilution 1:200), ct-H3 (Abcam, ab5103), Histone H3 (citrulline R2 + R8 + R17) Rabbit antibody - ChIP Grade (dilution 1:250) and MPO (R&D, cat#AF3667): Goat anti-myeloperoxidase (dilution 1:200) was used. For IMC studies Histone H3 Cell Signaling Technology 4499BF D1H2 17 1:400, FOXP3 Invitrogen 14-4777-82 236A/E7 2378013 1:25, CD4 Abcam ab181724 EPR6855 GR3285644-12 1:50, NKG2A Abcam ab273516 EPR23737-127 GR3410074-2 1:25, CD8a Dy162 eBioscience 14-0085-82 C8/144B 2132595 1:100, ARGI Cell Signalling 89872SF D4E3M 11:50, CD3 Fluidigm 3170019D Polyclonal. C-Terminal 2202221-161:100, TRDC Yb171 Santa Cruz sc-100289 H-41 L13211:50 and KRTS/18 Fluidigm 3174022D (513720071:100 were used.
Validation	All antibodies were validated for the purpose of our studies with positive and negative human control tissues, as well as IgG controls from the same species. In addition, all antibodies used are commercially available and validated according to manufacturer's websites, as stated below. Anti-Ki67 (SP6) is recombinant and abcam validated by knockout (https://www.abcam.com/products/primary-antibodies/ki67-antibody-sp6-ab16667.html). Anti-IBA-1 (https://labchem-wako.fujifilm.com/us/product_data/docs/00055446_doc02.pdf). Anti-CD45 (2B11) has been tested by Dako/Agilent with tonsil B and T cells as positive controls and brain microglia as negative controls (https://www.agilent.com/cs/library/catalogs/public/00230-d58532-02-atlas-of-controls-2nd-edition-agilent.pdf). Anti-p53 (DO7) was validated as shown in Supplementary Data Fig. 1 and according to manufacturer (https://www.agilent.com/en/product/immunohistochemistry/antibodies-controls/primary-antibodies/p53-protein-%28dako-omnis%29-76230). Anti-CD11B (EPR1344) was tested against human tonsil and sleep as stated on the manufacturer's website (https://www.abcam.com/products/primary-antibodies/cd11b-antibody-epr1344-ab133357.html). Anti-CD68 (KP1) was validated against multiple human tissues (https://www.agilent.com/en/product/immunohistochemistry/antibodies-controls/primary-antibodies/cd68-%28concentrate%29-76535). Anti-CD3 was validated by the manufacturer (https://www.agilent.com/en/product/immunohistochemistry/antibodies-controls/primary-antibodies/cd3-%28concentrate%29-76133). Anti-CD8 was validated according to manufacturer (https://www.cellsignal.com/products/primary-antibodies/cd8a-d4w2z-xp-rabbit-mab/98941). Anti-NE was

validated according to manufacturer (https://www.lsbio.com/pathplus-antibodies/pathplus-hne-antibody-neutrophil-elastase-antibody-elisa-ihc-ls-b4244/118639). Anti-ct-H3 was validated accoding to manufacturer (https://www.abcam.com/products/primary-antibodies/histone-h3-citrulline-r2--r8--r17-antibody-ab5103.html). Anti-MPO was validated according to manufacturer (https://www.rndsystems.com/products/human-mouse-myeloperoxidase-mpo-antibody_af3667). Anti-histone H3 (D1H2) was validated according to manufacturer (https://www.cellsignal.com/products/primary-antibodies/histone-h3-d1h2-xp-rabbit-mab/4499). Anti-FOXP3 was validated according to manufacturer (https://www.thermofisher.com/antibody/product/FOXP3-Antibody-clone-236A-E7-Monoclonal/14-4777-82). Anti-CD4 was validated according to manufacturer (https://www.abcam.com/products/primary-antibodies/cd4-antibody-epr6855-bsa-and-azide-free-ab181724.html). Anti-NKG2A was validated according to manufacturer (https://www.abcam.com/products/primary-antibodies/nkg2a-antibody-epr23737-127-bsa-and-azide-free-ab273516.html). Anti-CD8a (C8/144B) was validated according to manufacturer (https://www.thermofisher.com/antibody/product/CD8a-Antibody-clone-C8-144B-Monoclonal/14-0085-82). Anti-arginase-1 was validated according to manufacturer (https://www.cellsignal.com/products/primary-antibodies/arginase-1-d4e3m-8482-xp-174-rabbit-mab-bsa-and-azide-free/89872). Anti-CD3 (Fluidigm) was validated according to manufacturer (https://fluidigm.my.salesforce.com/sfc/p/#700000009DAw/a/4u0000019iHf/m23J6T1Co3D7DkuFRjJdXVy7kXUfOMaOh3pr2RZnNqI). Anti-TRDC is validated according to manufacturer (https://www.scbt.com/p/tcr-delta-antibody-h-41). Anti-KRT8/18 was validated according to manufacturer (https://fluidigm.my.salesforce.com/sfc/p/#700000009DAw/a/4u0000019iH6/Klv3TAc8ZlVEKmaFXZAy5E_i7KKlrKMau0uNZuiXzS8).

Clinical data

Policy information about clinical studies

All manuscripts should comply with the ICMJE guidelines for publication of clinical research and a completed CONSORT checklist must be included with all submissions.

Clinical trial registration	NCT02393703
Study protocol	A summary of the #15-015 study protocol, which includes additional investigations and endpoints not published here, is available on the ClinicalTrials.gov trial registration website. The full protocol is available on demand by contacting the corresponding authors.
Data collection	Data was collected from the study initiation (4/2015) until closure of followup in 12/2021.
Outcomes	The primary endpoint pertaining to this study was differences in the liver among patients with PaC and Non-PaC. The secondary outcome was hepatic differences between PaC patients with various patterns of recurrence, or no recurrence.

Plants

Seed stocks	*Report on the source of all seed stocks or other plant material used. If applicable, state the seed stock centre and catalogue number. If plant specimens were collected from the field, describe the collection location, date and sampling procedures.*
Novel plant genotypes	*Describe the methods by which all novel plant genotypes were produced. This includes those generated by transgenic approaches, gene editing, chemical/radiation-based mutagenesis and hybridization. For transgenic lines, describe the transformation method, the number of independent lines analyzed and the generation upon which experiments were performed. For gene-edited lines, describe the editor used, the endogenous sequence targeted for editing, the targeting guide RNA sequence (if applicable) and how the editor was applied.*
Authentication	*Describe any authentication procedures for each seed stock used or novel genotype generated. Describe any experiments used to assess the effect of a mutation and, where applicable, how potential secondary effects (e.g. second site T-DNA insertions, mosiacism, off-target gene editing) were examined.*